NEUROSCIENCE

A spatiotemporal complexity architecture of human brain activity

Stephan Krohn[1,2]*, Nina von Schwanenflug[1,2]†, Leonhard Waschke[3,4]†, Amy Romanello[1,2], Martin Gell[2,5,6], Douglas D. Garrett[3,4], Carsten Finke[1,2]*

The human brain operates in large-scale functional networks. These networks are an expression of temporally correlated activity across brain regions, but how global network properties relate to the neural dynamics of individual regions remains incompletely understood. Here, we show that the brain's network architecture is tightly linked to critical episodes of neural regularity, visible as spontaneous "complexity drops" in functional magnetic resonance imaging signals. These episodes closely explain functional connectivity strength between regions, subserve the propagation of neural activity patterns, and reflect interindividual differences in age and behavior. Furthermore, complexity drops define neural activity states that dynamically shape the connectivity strength, topological configuration, and hierarchy of brain networks and comprehensively explain known structure-function relationships within the brain. These findings delineate a principled complexity architecture of neural activity—a human "complexome" that underpins the brain's functional network organization.

INTRODUCTION

The human brain operates in large-scale functional networks that underpin cognition and behavior (*1*–*7*). Collectively subsumed as the functional human connectome (*8*, *9*), these networks are an expression of temporally correlated activity across spatially distributed brain regions. This covariance of neural signals is commonly referred to as functional connectivity (FC) (*10*–*12*), and the estimation of FC from functional magnetic resonance imaging (fMRI) has revealed important insights into the brain's functional architecture. First, FC is not uniformly distributed across the brain, but rather organized in functional subsystems known as resting-state networks (RSNs) (*2*, *5*–*7*, *13*). Second, FC is not static over time but shows dynamic fluctuations that result in distinct temporal network states (*14*–*18*). Third, the configuration of the network is not random, but follows an efficient topology thought to reflect communicational constellations within the network (*18*–*21*). Last, brain networks are not functionally uniform, but are organized along a principal hierarchy spanning from lower-order unimodal to higher-order transmodal processing systems (*22*–*24*).

Despite these advances, it remains a fundamental challenge in neuroscience to understand what determines the structure, temporal dynamics, and hierarchy within the human connectome. To achieve such an understanding, an explanatory framework is required which links this global network architecture to the local activity of individual brain regions. Such a link is critical because FC—and all network properties derived from it—are defined on the covariance relationship across regional signals. Given this directionality of network construction (regional activity defines interregional covariance, but not vice versa), the global properties of the network must ultimately be rooted in the neural dynamics of individual regions. To this effect, the variability of neural activity fluctuations gives rise to the covariance structure that defines the network (*6*, *25*–*28*), but how the global network architecture relates to the variability of local neural activity remains incompletely understood.

RESULTS

Brain activity is characterized by critical moments of neural regularity

To address this gap, we here use an information-theoretic complexity analysis that (i) relates the local activity of individual brain regions to the global properties of the network, (ii) represents the intrinsic variability of neural fluctuations in a standardized space, and (iii) allows for a time-resolved account of neural variability to capture the temporal dynamics within individual signals. This approach rests on symbolic encoding of blood oxygen level–dependent (BOLD) activity and leverages both amplitude information and the diversity of abstract patterns in the signal to quantify the degree of irregularity (i.e., signal complexity) over a given moment in time (figs. S1 and S2) (*29*). We thus obtain a complexity time series for each brain region, which captures local dynamics through a meta-representation of neural variability and allows for a link between the nodes in the network (i.e., individual regions) and the edges in the network (i.e., region-to-region functional connections).

Application of this approach to resting-state fMRI from the Human Connectome Project (HCP) (*8*) revealed a highly canonical complexity architecture of human brain activity: Over ~80% of the acquisition time, the brain exhibits widespread high-complexity signals, approaching the upper limit of expected values given the underlying signal characteristics (figs. S1 to S3). Intermittently, however, this high-complexity activity is interrupted by

[1]Charité-Universitätsmedizin Berlin, corporate member of Freie Universität Berlin and Humboldt-Universität zu Berlin, Department of Neurology, Berlin, Germany. [2]Berlin School of Mind and Brain, Humboldt-Universität zu Berlin, Berlin, Germany. [3]Center for Lifespan Psychology, Max Planck Institute for Human Development, Berlin, Germany. [4]Max Planck UCL Centre for Computational Psychiatry and Ageing Research, Berlin, Germany. [5]Institute of Neuroscience and Medicine (INM-7), Heinrich Heine University Düsseldorf, Düsseldorf, Germany. [6]Department of Psychiatry, Psychotherapy and Psychosomatic Medicine, RWTH Aachen University, Aachen, Germany.
*Corresponding author. Email: stephan.krohn@charite.de (S.K.); carsten.finke@charite.de (C.F.)
†These authors contributed equally to this work.

spontaneous "complexity drops" that correspond to episodes of increased regularity in the BOLD signal (Fig. 1A). Specifically, "regularity" here means that there are moments in the signal in which a dominant symbolic motif explains most of the relative amplitude variation in the time series, which is demonstrated for an exemplary BOLD window in the inset of Fig. 1A. Here, the relative amplitude variation in the exemplary thalamic region (top row) is largely split between an "upward" motif (1-2-3) and a "downward" motif (3-2-1). In contrast, in the left precuneus (bottom row), nearly all amplitude variance over the given window is attributed to the downward motif, resulting in a highly regular pattern distribution and thus in a drop in complexity over this window.

These complexity drops appear in clusters of brain regions and over well-delineated moments in time, and the number of brain regions exhibiting drops closely reflects the current overall complexity of neural activity. Notably, this complexity architecture was universally present in all analyzed recordings (684 scans from $n = 343$ participants; also see online repository for individual scans and validation in holdout data) and was highly robust against different windowing parameters, parcellation granularity, and time series extraction methods (figs. S4 and S5).

Spatial analysis revealed persistent high-complexity activity in medial temporal, anterior cingulate, and subcortical regions—most markedly in thalamic areas (Fig. 1B). In contrast, complexity drops predominantly occurred in the cortex, with a focus on pericentral regions. On the level of individual participants, the affinity for complexity drops was strongly linked to grand-average brain signal complexity ($r = -0.9$, $P = 1.6 \times 10^{-125}$) and showed significant differences across RSN [$\chi^2(7) = 154$, $P = 6.1 \times 10^{-30}$] as well as gradual decreases with age [$\chi^2(2) = 17.1$, $P = 1.9 \times 10^{-4}$], even over the narrow age range of early adulthood (Fig. 1B).

This time-resolved representation of BOLD dynamics subsequently allowed us to relate the complexity time series of individual regions to the FC between those regions. Analyzing the co-occurrence of complexity drops across the brain revealed that FC strength between any two regions is strongly associated with the degree to which they exhibit complexity drops together (Fig. 1C). While this "drop coincidence" explained a large part of the variance in FC overall ($F_{1,30133} = 4.3 \times 10^4$, $P \approx 0$, $R^2_{adj} = 0.59$), it was also significantly higher for connections within, rather than across, canonical RSNs ($W = 3.6 \times 10^7$, $P = 9.3 \times 10^{-161}$), paralleled by higher within- than across-network connectivity.

A further link to such network differentiation is demonstrated by the interhemispheric symmetry of regional complexity time series (Fig. 1D), quantified as the rank-weighted correlation of each region with its contralateral equivalent. This interhemispheric symmetry was systematically constrained by canonical RSNs [$\chi^2(7) = 169$, $P = 4.6 \times 10^{-33}$] and intrinsically mirrored the recently uncovered hierarchy between unimodal and transmodal areas (*22*, *23*), suggesting that the cross-hemispheric coupling of neural activity patterns is strongest in primary networks and becomes gradually more diverse in higher-order systems.

Notably, these complexity dynamics are not simply explained by covariation in signal amplitudes across regions and are specifically distinct from BOLD cofluctuations as defined by the recently reported edge time series (fig. S6) (*30*, *31*). Instead, associations between complexity dynamics and BOLD cofluctuations are consistently small to near zero, both in the case of continuous time series

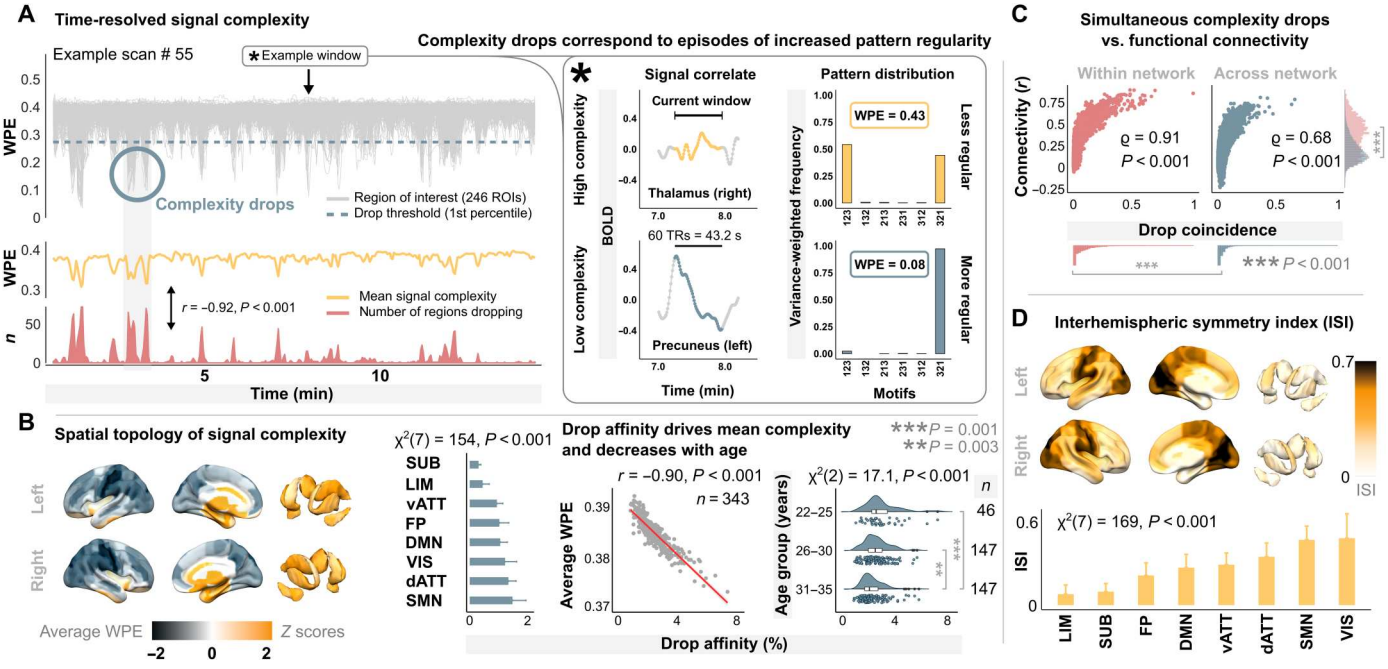

Fig. 1. Human brain activity is characterized by critical moments of neural regularity that are visible as transient complexity drops. (**A**) Time-resolved WPE on the neural signals from each ROI in an exemplary resting-state recording (Brainnetomeparcellation; window length of 60 TRs, 95% overlap). The inset displays the BOLD correlates of two representative high- and low-complexity signals. (**B**) Spatial distribution of average signal complexity. Drop affinity over RSNs, link to grand-average signal complexity, and age-related reduction in drop affinity. (**C**) FC as a function of drop coincidence, within and across canonical RSNs. (**D**) Spatial topology and network distribution of interhemispheric complexity symmetry. dATT, dorsal attention; DMN, default mode; FP, frontoparietal; LIM, limbic; SMN, somatomotor; SUB, subcortical; vATT, ventral attention; VIS, visual network.

(BOLD cofluctuation amplitude versus complexity cofluctuation amplitude) and in the case of event time series (high-amplitude BOLD cofluctuation events versus drop coincidences).

Similarly, a null model of temporal dependency that preserves signal means, amplitude variance, and FC (*32*) showed a pronounced disruption of both the spatiotemporal organization of signal complexity across the brain and of interindividual differences across participants (fig. S7). In particular, we observed a dissolution of the spatial complexity topology in Fig. 1B (left), the individual affinity for complexity drops including the age effect (Fig. 1B, right), and the propensity of brain regions to drop together at the same time (Fig. 1C), even when the absolute number of complexity drops in the surrogate data was enforced to be the same.

Moments of regularity spread throughout the brain

Recent work has suggested a propagation of BOLD activity patterns throughout the brain as a means of communication within the network (*33*–*35*). As the symbolic encoding approach used here inherently captures such neural patterns (*29*), we asked whether complexity drops may reflect the propagation of neural activity across the brain. Supporting this idea, complexity drops consistently occurred in dynamic cascades that start with a few initializing regions, gradually spread across the brain, and finally fade back to a few regions again such that brain-wide drop engagement exhibits an inverted U-shape over time (Fig. 2A and movie S1). Such cascades were present in all 343 participants and typically lasted for about 10 s (mean duration, 9.4 ± 3.5 s; range, 6.5 to 41 s). To analyze the spread of complexity drops across the brain, we developed a graph theoretical framework, where each individual propagation is described by a directed graph (Fig. 2B). These propagation graphs contain node layers that represent consecutive BOLD windows from initialization of the cascade ("source layer") to maximum drop engagement ("peak layer"), and where the direction of edges expresses progression in time, allowing for the estimation of region-to-region transition probabilities within the propagation.

Drop cascades were characterized by a strong positive relationship between cascade duration and the number of regions engaging in them ($\rho = 0.79$, $P_{adj} = 2.9 \times 10^{-73}$), and the number of cascades an individual presented was strongly related to their source diversity, defined as the proportion of unique brain regions ever initializing a cascade ($\rho = 0.96$, $P_{adj} = 2 \times 10^{-182}$; Fig. 2C). Notably, we observed significant age-related reductions in the number of cascades [$\chi^2(2) = 13.9$, $P = 9.5 \times 10^{-4}$] and in source diversity [$\chi^2(2) = 16.3$, $P = 2.8 \times 10^{-4}$], but not in the number of regions dropping [$\chi^2(2) = 4.5$, $P = 0.11$] or cascade duration [$\chi^2(2) = 2.6$, $P = 0.27$], suggesting that individual propagations occur in a semicanonical fashion, although the predisposition to engage in them decreases with age (Fig. 2C).

Spatial analysis of propagation graphs revealed that drop cascades originate predominantly in the cortex, with a focus on lower-order RSNs (Fig. 2D). Furthermore, graph construction from the transition probabilities of individual spreads uncovered a highly structured spatiotemporal propagation network (Fig. 2E). Centrality analysis on this network revealed that the propagation of complexity drops across regions follows an intrinsic hierarchy

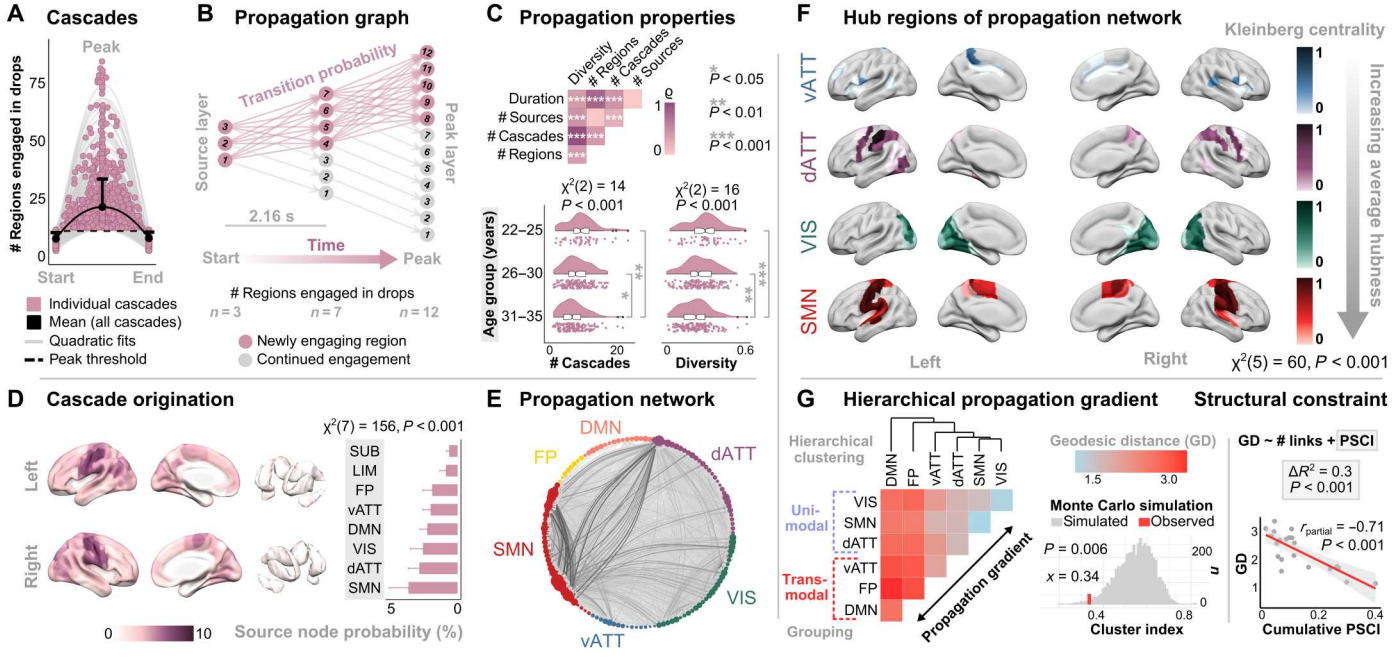

Fig. 2. Complexity drops spread throughout the brain along a principal functional hierarchy. (**A**) Drop cascades. Points represent a random sample of 500 out of 5279 total cascades in the study population. Cascades are thresholded to at least 10 regions dropping simultaneously at peak. (**B**) Formalization of individual spreads as directed propagation graphs. Window-to-window temporal resolution corresponds to 2.16 s (3 TRs). (**C**) Propagation properties and age effects (pairwise tests FDR-corrected). (**D**) Spatial topology of cascade origination. (**E**) Propagation network, thresholded to the 95th percentile of strongest connections (edge thickness: transition probability; node diameter: source probability). (**F**) Hub topology of the thresholded propagation network, given by Kleinberg's eigenvector centrality. FP and DMN are omitted because of near-zero entries only. (**G**) Average node-to-node geodesic distances in the propagation network. Monte Carlo simulation testing the significance of unimodal versus transmodal network clusters. Association between geodesic distances and structural connectivity. PSCI, probabilistic streamline connectivity index.

(Fig. 2F), where the most influential nodes correspond to primary RSNs, and nodes of higher-order systems become gradually less important to the propagation.

Further supporting such a propagation hierarchy from lower-order to higher-order systems, geodesic distances between all node pairs in the propagation network were calculated to describe how likely it is for a complexity drop to spread from one region to another. These geodesics showed that complexity drops spread along spatiotemporal pathways that exhibit a unimodal-to-transmodal functional gradient (Fig. 2G), assessed by Monte Carlo simulation of the cluster groups ($x_{cluster} = 0.34$, $P = 0.006$; see Materials and Methods for test details). This propagation structure thus again strongly converged with the functional hierarchy within the connectome (*22*–*24*), characterized by a principal gradient between lower-order unimodal and higher-order transmodal processing systems.

Given this link between drop propagations and functional networks, we furthermore asked whether the spread of complexity drops from one region to another was additionally constrained by the structural connectivity between them. In line with this idea, modeling geodesic distances as a function of probabilistic streamline connectivity and the number of structural links ($R^2_{adj} = 0.66$, $F_{2,18} = 20.9$, $P = 2 \times 10^{-5}$) significantly improved explanatory power ($\Delta R^2 = 0.3$, $\eta^2_{partial} = 0.5$, $F_{1,18} = 17.8$, $P = 5.1 \times 10^{-4}$) compared to when only the number of links was considered ($R^2_{adj} = 0.37$, $F_{1,19} = 12.7$, $P = 0.002$), suggesting that drop propagation across regions is further constrained by structural connectivity.

Neural activity is organized in network-modulating complexity states

Next, we related the complexity dynamics of individual regions to the behavior of the whole-brain network, testing the idea that temporal network states (*14*, *15*, *18*) (i.e., functional states of the edges) are rooted in underlying activity states of the neural signals from which the network is estimated (i.e., functional states of the nodes). Unsupervised structure detection with *k*-means clustering on the complexity time series supported this idea, showing that neural signals are organized in distinct temporal complexity states (Fig. 3A; see Materials and Methods for parameter details). Consistent with the inspection of individual time series (Fig. 1A; online repository), participants spent most time in a default neural state of high complexity, while the more infrequently visited states entailed gradually decreasing levels of complexity, yielding a strong discriminative effect of complexity across temporal states ($\eta^2 = 0.90$, [0.89 to 0.91]). Notably, while complexity states are derived directly from the activity of individual brain regions, they resulted in pronounced concomitant effects on the connectivity strength and topological configuration of the connectome, which are derived from region-to-region signal correlations. In particular, the default state of neural activity is characterized by low connectivity strength of the network, while the lower-complexity states entail gradual increases in connectivity (Fig. 3A).

This impact of complexity states furthermore extended to the topological configuration of the connectome (*3*, *19*, *20*), with the default neural state yielding high modularity and low efficiency in the network. As for FC, visiting lower-complexity states entailed gradual decreases in modularity and concomitant increases in network efficiency. Notably, this network-modulating effect of complexity states even held at the temporal resolution of individual window-to-window transitions (Fig. 3B). While all complexity states were similarly stable, switches between low-complexity and high-complexity brain states typically occurred through the intermediate states, and these transitions were accompanied by fine-grained, momentary changes in the connectivity, modularity, and efficiency of the network.

Given these group-level effects of complexity states on the ne twork, we furthermore tested how much the space of possible complexity states was explored by individual participants (Fig. 3C). To this end, we derived a measure of state exploration based on the Wasserstein distance between an individual's empirical state visits and a theoretical uniform distribution. This state dispersion index (SDI) was consistent across two consecutive days of scanning ($\rho = 0.51$, $P \approx 0$) and significantly decreased with age [$\chi^2(2) = 12.8$, $P = 0.002$], suggesting that older participants present increasingly rigid neural dynamics, consistent with the age-related reductions in drop affinity (Fig. 1B) and propagation diversity (Fig. 2C). Notably, all state-related findings were highly robust against the number of expected complexity states as defined by the clustering parameters (figs. S8 and S9).

Complexity states link structural and functional network hierarchies

Next, we analyzed how these neural complexity states are spatially embedded in the brain. Given that both interhemispheric signal coupling (Fig. 1D) and the propagation of complexity drops (Fig. 2, E to G) intrinsically followed the principal unimodal-to-transmodal hierarchy, we explicitly estimated the corresponding gradient loadings from the FC data and related them to the topology of complexity states. Furthermore, these gradient loadings have been shown to be spatially correlated with cortical myeloarchitecture as a proxy of anatomical hierarchy (*22*, *36*, *37*), yielding an important structure-function relationship within the connectome (*38*) that also partly extends to nonprimate mammalian brains (*39*, *40*). Thus, we estimated cortical myelination as the T1-weighted/T2-weighted image ratio and related this myelin distribution to the functional gradient loadings and complexity states.

The topology of complexity states corroborated the distribution of average signal complexity (Fig. 1B), with subcortical areas consistently showing high-complexity activity, largely independent of the current global complexity state (Fig. 4A). In contrast, cortical topologies varied distinctly with the number of regions exhibiting complexity drops [$\chi^2(3) = 1172$, $P = 9.4 \times 10^{-254}$], inducing significant spatial heterogeneity across states [modified likelihood ratio test (MLRT) = 655, $P \approx 0$]. Furthermore, note that the topologies in Fig. 4A correspond to within-state *z* scores and thus represent the relative regional complexity distribution in each state. In contrast, fig. S10 depicts the absolute complexity values over states, regions, and participants, showing that the identified states are distinct—in line with the significant differences in complexity drops over states (Fig. 4A, right)—even when the within-state topologies show similar patterns (e.g., states 3 and 4).

To estimate which brain regions may drive these differences, we defined a measure of distance across complexity states (DACS) as the cumulative centroid-to-centroid Euclidean distance for every region across four-dimensional state space (Fig. 4B). Again, the DACS topology closely followed a unimodal-to-transmodal gradient, where regions that were most variable across complexity states represented the unimodal end of the hierarchy. Testing this spatial

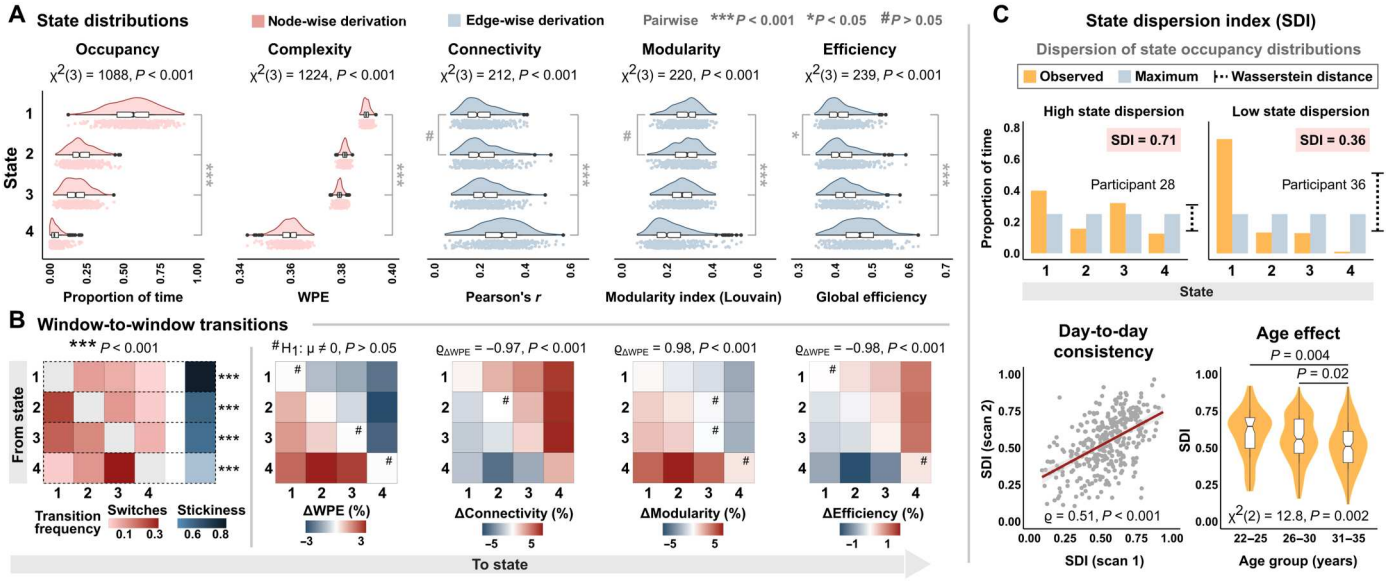

Fig. 3. Neural activity is organized in temporal complexity states that modulate network strength and configuration. (**A**) State-wise distributions of occupancy, signal complexity, connectivity strength, network modularity, and global efficiency. Points represent participants ($n = 343$). Node-wise derivation refers to estimation from individual regional signals, and edge-wise derivation refers to estimation from the network (i.e., region-to-region correlations). (**B**) Window-to-window state transition frequencies. State-dependent changes tested against deviation from zero (*t* test, $P_{FDR} < 0.05$ for all except those marked by #). Association of network measures with ΔWPE corresponds to the correlation of the respective matrices. (**C**) Illustration, consistency across two consecutive days, and age-related reduction of the state dispersion index (SDI).

convergence with spin permutation correlation uncovered a pronounced positive association of DACS topology with cortical myeloarchitecture ($\rho_{empirical} = 0.67$, $P_{spin} < 0.001$) as well as a strong negative relationship with the connectivity gradient ($\rho_{empirical} = -0.76$, $P_{spin} < 0.001$; Fig. 4C).

While we were able to replicate the previously reported link between myelination and the FC gradient (*36*) ($\rho_{empirical} = -0.52$, $P_{spin} < 0.001$), partial correlations of all three variables revealed that the association between myelin and the gradient loadings disappears when controlling for complexity, whereas the complexity-myelin and complexity-gradient relationships persist when controlling for the respective other variable (Fig. 4D). Further corroborating this finding, a hierarchical regression approach showed that the complexity topology alone explained a large part of the variance in gradient loadings ($R^2_{adj} = 0.57$, $P = 4.9 \times 10^{-40}$) and that accounting for complexity in the augmented model completely resolves the myelin-gradient effect (Fig. 4D).

Complexity states reflect structure-function coupling in brain networks

Given the explanatory power of complexity states in accounting for structure-function relationships, we furthermore related the spatial embedding of Fig. 4B to a recent method by Preti and Van De Ville (*41*) that quantifies how strongly structure and function are coupled in a given brain region. Specifically, this structure-function decoupling index (SFDI) measures the dependency of a brain region's activity on anatomical connections by projecting the functional signals onto structural-connectome harmonics (*41*). Figure 5A illustrates this approach and shows the spatial distribution of structure-function coupling over regions, as computed from our dataset. This topology closely replicates the spatial distribution found by Preti and Van De Ville, with stronger structure-function coupling in sensory-motor regions and lower structure-function coupling in higher-cognitive areas. Furthermore, relating this distribution to the spatial topology of complexity states revealed a multimodal gradient of macroscale cortical organization (Fig. 5B) that links structural connectivity, FC, and local neural dynamics. In this gradient, one end comprises regions that show many complexity drops, are highly variable over complexity states, represent the unimodal end of the functional hierarchy, and show high structure-function coupling. In contrast, the opposing end includes regions that show fewer complexity drops, are less variable over complexity states, represent the transmodal pole of the functional hierarchy, and show lower structure-function coupling.

Complexity dynamics are highly consistent in holdout data

Validation analyses in holdout data from the same participants showed that the distribution of signal complexity was remarkably consistent compared to the main analyses (see fig. S11 for a quantile-quantile plot), yielding almost identical drop thresholds (Fig. 6A). Despite being highly dynamic metrics, the affinity of individual participants for complexity drops as well as their mean signal complexity were strongly correlated in main and holdout data (Fig. 6B). Moreover, independent clustering on the holdout data closely corroborated the distribution of neural complexity states, yielding a dominant high-complexity state and gradually more infrequent lower-complexity states (Fig. 6C), as in the main analyses. Furthermore, the degree to which complexity states were explored by participants (measured by the SDI) as well as the spatial embedding of complexity states in the brain (measured by the DACS) were also highly consistent in holdout data (Fig. 6D).

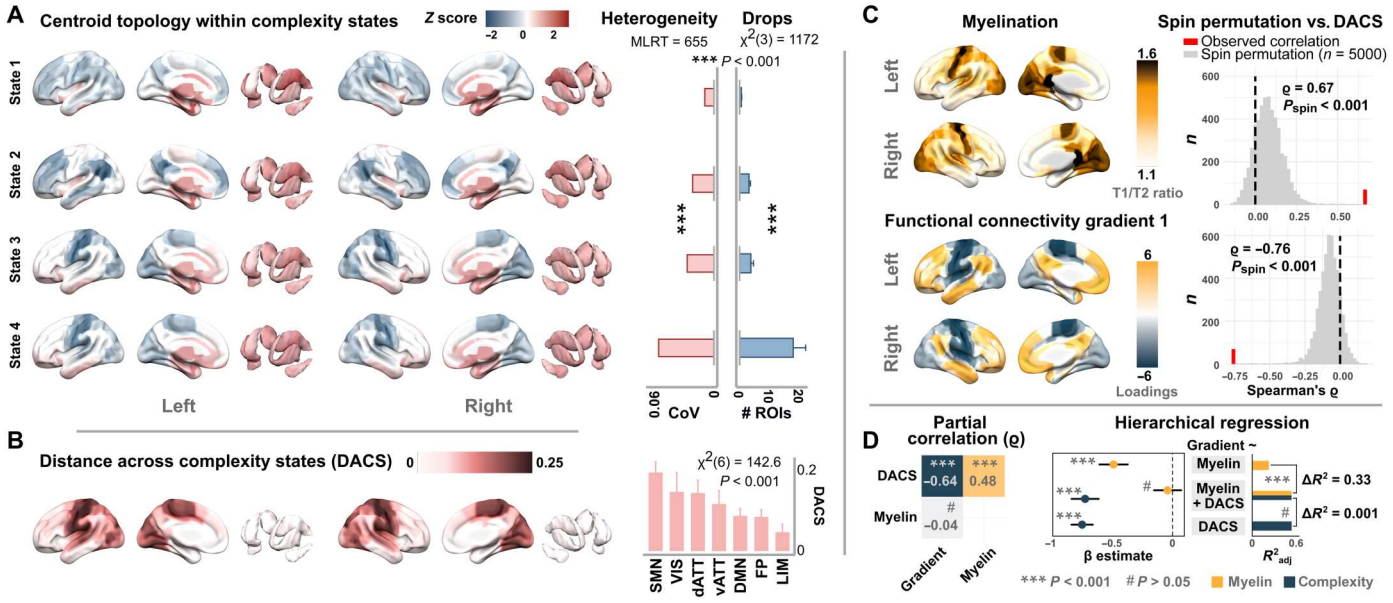

Fig. 4. The spatial embedding of complexity states comprehensively explains structure-function relationships within the brain. (**A**) Spatial topology of centroid locations (within-state *z* scores). Coefficient of variation (CoV) over regions and average number of complexity drops per state (error bars: SD). (**B**) Spatial topology and network distribution of the distance across complexity states (DACS). (**C**) Average regional myelination (proxied by T1-weighted/T2-weighted image ratio) and the primary unimodal-to-transmodal FC gradient. Correlation to the DACS assessed by spin permutation tests. (**D**) Partial correlation between complexity, myelin, and the connectivity gradient. Hierarchical regression on the gradient loadings with myelin content and the DACS as explanatory variables. All pairwise tests were FDR-corrected.

Complexity-behavior associations

Last, we investigated the behavioral implications of the observed complexity dynamics, given that neural variability is increasingly recognized to carry important functional significance (*28*, *42*). On the basis of the age-related reduction in drop affinity (Fig. 1B) and the link between complexity drops and functional integration (Fig. 3, A and B), we expected lower complexity values to reflect better behavioral performance and lower age. To test this relationship, participant age and behavioral variables were subjected to a multivariate partial least squares (PLS) analysis, including composite scores of crystallized and fluid abilities and the first principal components of individual cognitive, motor, and sensory task performance metrics (fig. S12). Furthermore, we conducted these analyses separately for the main dataset and the holdout data (Fig. 7) as well as individual scanning sessions (fig. S13) to estimate the consistency of behavioral effects. PLS returned a significant latent solution on the relationship between variance in complexity and differences in behavior (permuted P value for main data: $P = 0$; holdout data: $P = 0.001$). Supporting directional expectations, latent brain scores were positively related to latent behavioral scores (main: $\rho = 0.28$; holdout: $\rho = 0.24$), and in this latent space, neural complexity was positively linked to age and negatively associated with fluid and crystallized abilities, cognitive task performance, and motor function, with high consistency across main and holdout data (Fig. 7, A and C). Furthermore, the associated bootstrap ratios (BSRs) showed that complexity-behavior associations were systematically constrained by functional networks [main: $\chi^2(7) = 95.4$, $P = 9.5 \times 10^{-18}$; holdout: $\chi^2(7) = 84.1$, $P = 2 \times 10^{-15}$], with strongest contributions by areas pertaining to the ventral attention and default mode network, and this effect was equivalently observed for main and holdout data (Fig. 7, B and D). While complexity-behavior associations were thus remarkably consistent across main and holdout data (where signal complexity was averaged over two scanning sessions, respectively), these findings also held at the level of individual scanning sessions, both in terms of age and behavioral effects and in terms of the spatial distribution of BSRs (fig. S13).

DISCUSSION

Collectively, these findings delineate a unifying principle of brain organization, grounded in a spatiotemporal complexity architecture of neural activity. This human "complexome" closes the gap between the variability of neural signals and several key properties of functional brain networks, with five immediate implications for our understanding of large-scale brain dynamics.

First, we show that resting-state brain activity is characterized by critical moments of neural regularity. Through time-resolved representation of regional BOLD dynamics, these episodes become visible as transient complexity drops that are ubiquitously observed across scanning sessions, participants, and a variety of methodological parameters. Notably, complexity drops occur spontaneously, are highly orchestrated over both time and space, and closely explain the connectivity strength of functional connections as the degree to which brain regions exhibit them simultaneously. In addition, simultaneous complexity drops strongly differentiate between connections within and connections across canonical RSNs, suggesting that functional subsystems are an expression of specific sets of regions dropping together particularly often. While these findings align well with the notion that functional connections are related to critical moments of neural activity (*17*, *30*, *43*), they also characterize FC as a graded rather than an exclusively event-like process (*44*). Although we find that regions show significant preference for dropping together with regions of their own

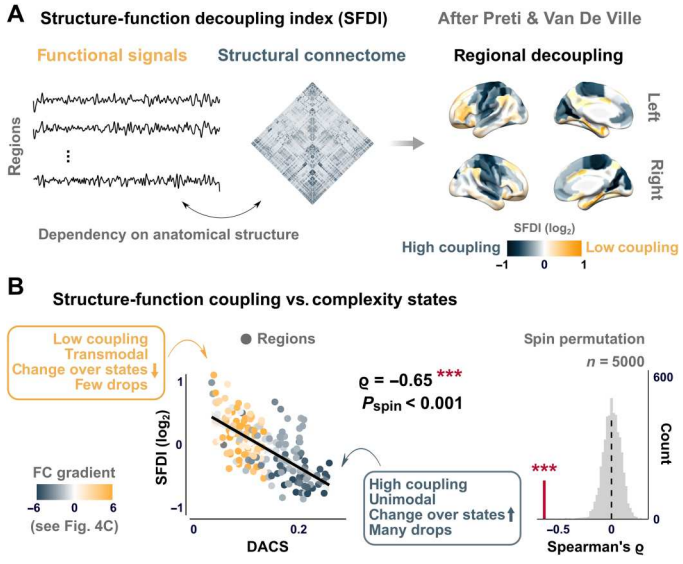

Fig. 5. Complexity states reflect structure-function coupling in brain networks. (**A**) Illustration of the SFDI defined by Preti and Van De Ville (*41*). The brain map on the right corresponds to the SFDI values computed from our dataset, displayed as the binary logarithm as in (*41*). Note that the SFDI measures decoupling such that negative values reflect higher structure-function coupling and positive values represent lower structure-function coupling. (**B**) Association between structure-function coupling and the DACS from Fig. 4B. Points represent brain regions and are colored according to the FC gradient loadings from Fig. 4C, reflecting the unimodal-versus-transmodal hierarchy. Significance of the empirical correlation was tested with spin permutation.

canonical network, there is also substantial drop coincidence among regions that are traditionally assigned to distinct functional networks (*13*), supporting the idea that brain regions can dynamically participate in different functional communities at different times (*45*, *46*). Notably, these complexity dynamics were markedly distinct from BOLD cofluctuations as defined by the recently reported edge time series (*30*) and were dissolved in a null model that explicitly preserved the covariance structure across regions (i.e., the FC matrix). This illustrates that the empirically observed link between connectivity and complexity is not a theoretical necessity—complexity drops can explain covariance, but covariance alone cannot explain complexity drops. Instead, our approach rather uncovers a unique perspective on neural dynamics by describing brain activity through the information-theoretic notion of complexity (*47*).

Second, we show that complexity drops link two key phenomena of human brain activity: the dynamic propagation of neural patterns and the functional hierarchy of large-scale brain networks. While we observe that complexity drops can generally start anywhere in the brain, they consistently spread across the cortex along highly structured spatiotemporal propagation pathways. These propagation pathways intrinsically exhibit a principal hierarchy between unimodal systems that are central to the propagation and transmodal systems that are less central to the propagation and tend to be their end points. Given that pattern propagation is thought to represent interregional communication (*35*, *48*), our results suggest that such large-scale communication across brain networks may itself be hierarchical in nature, consistent with computational theories on information processing in the brain (*49*) and a recent framework on bidirectional information flow among brain regions (*50*). Furthermore, recent work has reported global arousal waves that similarly propagate from extrinsic, sensorimotor brain systems to intrinsic, higher-order systems, presumably reflecting spatiotemporal patterns of brain-wide excitability (*51*). Although these reports were based on phase characteristics of the signal rather than amplitude-weighted neural patterns, the similarity of propagational pathways raises the possibility that moments of regularity could be linked to arousal-related states of excitability. Notably, the propagation of complexity drops also aligns well with the recently reported activity pulses in disused motor circuits (*52*), which likewise occurred spontaneously and intrinsically spread through the motor network. Our results suggest that these pulses may represent an adaptive enhancement of a preexisting phenomenon—the dynamic propagation of regularity throughout the brain. Given our finding that these propagations inherently follow a principal functional hierarchy, such episodes may not be limited to impairment-induced plasticity (*52*) but rather represent a more general mechanism by which the brain repeatedly and intrinsically self-maintains its functional architecture.

Third, we show that complexity drops define temporal states of neural activity and that these neural complexity states dynamically modulate the connectivity strength and topological configuration of the network in a moment-by-moment fashion. Given the directionality of network construction—the covariance across neural signals is what defines the network in the first place—it is expected that local activity states should underlie the temporal states of the global network. In this regard, we find that the more infrequent low-complexity states yield a network constellation of high connectivity, low modularity, and high efficiency, consistent with previous findings on network topology dynamics (*18*, *21*). In particular, we not only corroborate the observation of temporary increases in network efficiency by Zalesky *et al.* (*18*) but also relate these increases to local neural dynamics by showing that they correspond to moments in which many regions drop at the same time.

In contrast, we found the default state of neural activity to be a high-complexity state with precisely the inverse network configuration (i.e., low connectivity, low efficiency, and high modularity). Notably, modularity and efficiency represent two complementary network characteristics, where the former describes a segregated configuration thought to reduce biological cost and the latter implies an integrated configuration that enhances communication within the network (*3*). The brain must balance both, however, yielding a cost-efficiency trade-off that is continuously renegotiated (*20*). Consequently, our findings indicate that the brain may implement such a trade-off with a default neural state of segregated activity that maintains cost-effectiveness, while the more infrequent low-complexity states ensure recurrent phases of functional integration.

Fourth, we show that the spatial embedding of complexity states comprehensively explains a well-established structure-function relationship in the brain (*38*): the association between connectivity gradient loadings as a proxy of functional hierarchy (*22*, *23*) and cortical myelination as a proxy of anatomical hierarchy (*22*, *36*, *53*). Notably, accounting for complexity states completely absorbed this effect, whereas the complexity-myelin and complexity-gradient relationships persisted, showing that local anatomical properties and distributed functional properties of the brain are linked through local functional dynamics. Similarly, the association between a brain region's complexity dynamics and the degree to

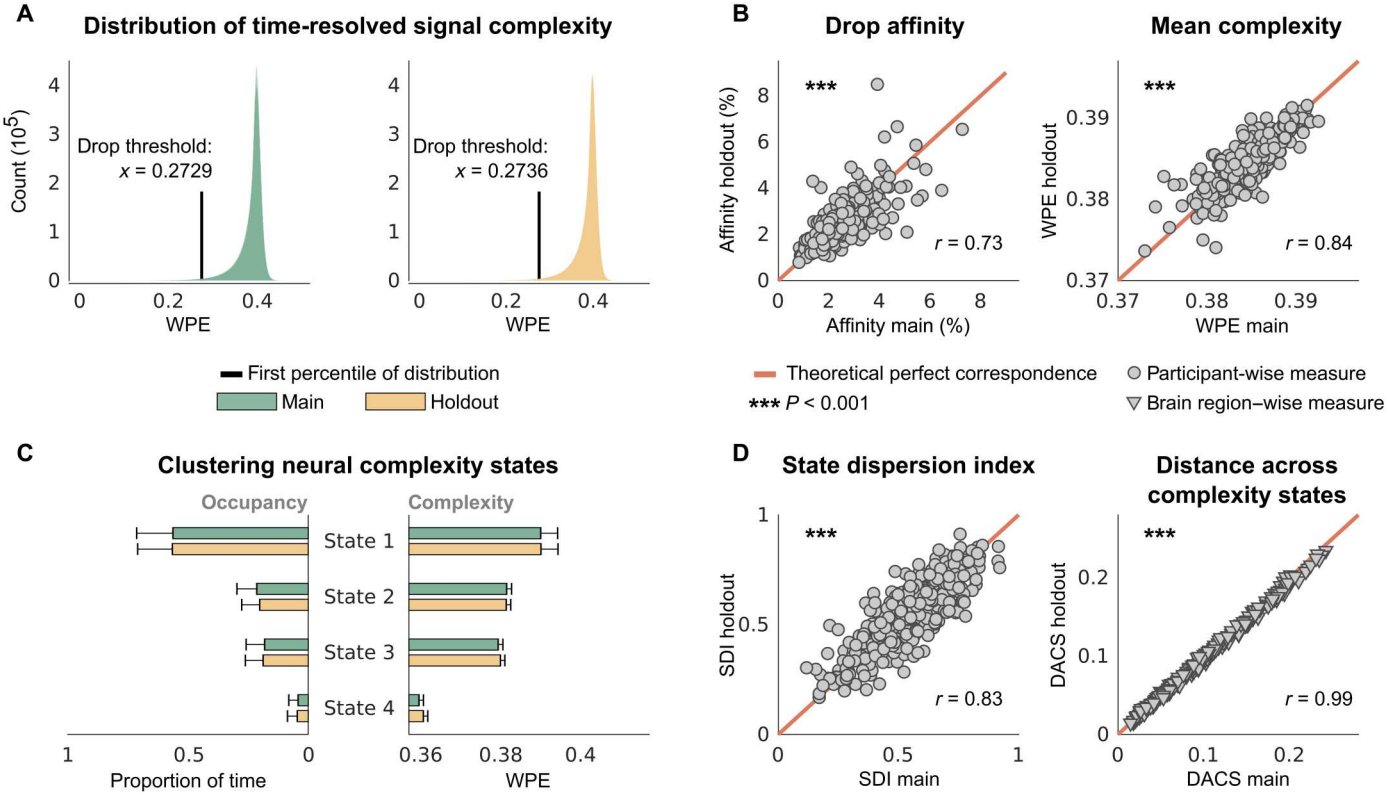

Fig. 6. Complexity measures are highly consistent in holdout data. (**A**) Distribution of time-resolved BOLD signal complexity in main and holdout data, resulting in nearly identical drop thresholds. (**B**) Consistency of participant-wise affinity for complexity drops and mean signal complexity (see Fig. 1B). (**C**) State occupancy and state-wise signal complexity derived from independent clustering of neural complexity states in holdout data (see Fig. 3A). Error bars represent SD. (**D**) Consistency of complexity state exploration as measured by the SDI (see Fig. 3C) and the spatial embedding of complexity states as measured by the DACS (see Fig. 4B).

which it exhibits structure-function coupling (*41*) revealed a multimodal gradient of cortical organization that links structural connectivity, FC, and local neural variability.

Last, we show that the observed complexity dynamics carry a number of interindividual functional implications that were robust across the main dataset, the holdout dataset, and individual scanning sessions. On the one hand, we find several pronounced effects of participant age, including age-related reductions in (i) the affinity for complexity drops, (ii) the magnitude and diversity in how complexity drops are propagated throughout the brain, and (iii) the degree to which participants explore the space of neural complexity states. These findings suggest that neural dynamics grow increasingly more rigid with age, even over the narrow age range of early adulthood (22 to 35 years). On the other hand, these age effects are paralleled by an inverse association between brain signal complexity and indices of cognitive and motor performance, with strongest contributions by areas pertaining to the ventral attention network. Given that (i) an individual's drop affinity strongly relates to overall signal complexity and age, (ii) complexity drops are tightly linked to phases of functional integration, and (iii) the ventral attention network is thought to act as an intermediary system for switching between networks, these results suggest that a higher capacity for complexity drops may represent a beneficial aspect of brain functioning.

Technical considerations

Some methodological considerations regarding the quantification of signal complexity from fMRI data deserve mentioning. On the one hand, the HCP data were acquired with a comparatively short time of repetition (TR = 0.72 s), yielding a subsecond temporal resolution that is not necessarily achieved in traditional protocols. While this acquisition was ideal for our approach of time-resolved complexity analysis, further work is necessary to understand how the rate at which brain activity is sampled may relate to the estimation of neural patterns from those samples.

Furthermore, the spatial distribution of signal complexity revealed consistent high-complexity activity in medial temporal and subcortical areas, whose time series typically show lower signal-to-noise ratios (SNRs) in fMRI recordings. While an influence of SNR on complexity estimation cannot be completely discarded, several considerations indicate that high signal complexity in these areas may not solely be an artifact of SNR. First, even across brain areas that are less prone to low SNR, high-complexity signals are by far the dominant part of the resting-state scan—their mean complexity is simply lower because they show more complexity drops. Conversely, complexity drops in high-complexity areas do occur consistently, just comparatively less often than in the rest of the brain. Furthermore, note that weighted permutation entropy (WPE) factors in the relative, not the absolute, amplitude variation (and is thus invariant to linear transformations), making it less prone to variations in SNR, which is commonly defined on absolute

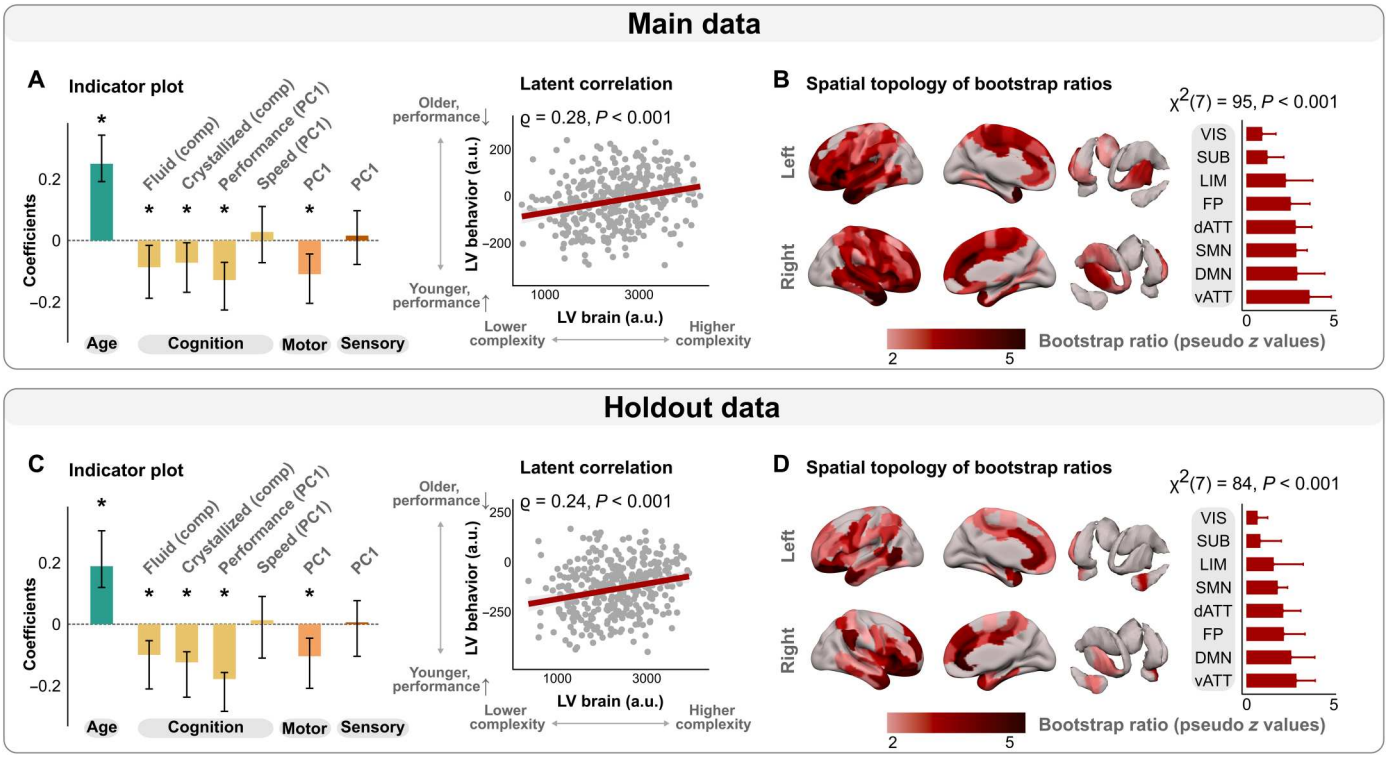

Fig. 7. Neural complexity reflects interindividual differences in age and behavior. Multivariate PLS analysis for the main (A and B) and holdout datasets (C and D). (**A**) Indicator plot for age and behavioral variables (error bars represent 95% confidence intervals; comp, composite score; PC1, first principal component; asterisks indicate significant coefficients). Correlation of brain and behavior scores of the first latent variable (LV). (**B**) Spatial topology and network distribution of the corresponding BSRs. (**C**) Indicator plot and latent correlation for the PLS analysis in the holdout data. (**D**) Spatial topology and network distribution of the BSRs in the holdout data. For unthresholded maps, see fig. S13. a.u., arbitrary units; BSR, bootstrap ratio.

amplitude magnitude. Notably, WPE was explicitly shown to be less sensitive to lower SNR than preceding measures when it was first proposed (*29*). Nonetheless, a systematic evaluation of the relationship between SNR and complexity estimation is certainly worthwhile, as the approach is further explored.

Last, given that complexity drops were ubiquitously present across participants and a range of methodological parameters, we investigated whether the empirically observed complexity dynamics would also be present in a null model of temporal dependency that preserves the FC structure across regions, and we observed a pronounced attenuation of spatial, temporal, and interindividual complexity effects in the surrogate data. While the temporal dependency of neural variability was precisely the focus of the current study, there is increasing interest in the question of which null model to define under different analytic approaches (*32*, *54*) such that it will be interesting to see how the empirical complexity dynamics may relate to other surrogate approaches incorporating different properties such as (higher-order) autocorrelation structures.

Future directions

Overall, the findings of this study lay out a coherent general framework that maps regional neural dynamics to functional brain networks, with some key future questions readily following. First, the age effects observed in young adults raise the question of how complexity dynamics develop over the larger life span, including infancy, adolescence, and late adulthood. Similarly, the complexome provides a principled normative account to describe brain activity, with immediate opportunities to study clinical populations and altered mental states. Moreover, the present study focuses on resting-state brain activity as assessed by fMRI, warranting further study on how complexity dynamics change during cognitive task engagement and what the correlates of complexity drops are in electrophysiological recordings with higher temporal resolution. Furthermore, complexity dynamics were highly stable within participants, raising the question of how these dynamics relate to individual functional "fingerprints" (*55*, *56*) and precision mapping of individual brain organization (*57*). Additionally, the present results ultimately call for a biological model that characterizes the physiological underpinnings of complexity drops and addresses the question of which specific biological function these episodes of neural regularity might serve. In light of our findings, one intriguing possibility could be that these moments represent a mechanism of self-maintenance by which the brain upholds its functional architecture through recurrent reiteration. A first step in addressing these questions may be to study whether the observed complexity dynamics are unique to the awake state or whether and how they may be altered during sleep or general anesthesia. In summary, our study speaks to a model of the brain in which its intricate functional architecture is tightly linked to moments of neural regularity, with several immediate implications for our understanding of large-scale brain dynamics.

MATERIALS AND METHODS

Data and preprocessing

Data were obtained from the HCP (*8*, *58*), including minimally processed resting-state fMRI (*58*, *59*), diffusion-weighted images, and T1-weighted/T2-weighted image ratios (*53*) as well as demographics and behavioral scores from 343 participants (205 females, 138 males). The HCP protocol was approved by the local Institutional Review Board of Washington University in St. Louis, MO, USA. For all participants, verbal informed consent was acquired during screening, and written informed consent was obtained at the beginning of the first study day (*8*). MRI data were acquired on a 3-T scanner at Washington University with multiband echo-planar imaging (1200 volumes, TR = 0.72 s, 2-mm isotropic voxels). Two runs of approximately 15 min each, one with right-to-left (RL) and one with left-to-right (LR) phase encoding protocol, were acquired on two consecutive days, resulting in a total of four resting-state datasets per participant. Spatial distortion correction was applied as provided in the HCP (*58*). Of the four scans, one encoding direction was chosen at random for days 1 and 2, respectively, resulting in two scans per participant with balanced phase encoding distribution for the main analyses (day1-LR: n = 168, day1-RL: n = 173, day2-LR: n = 166, day2-RL: n = 177; Pearson's χ^2 test: $\chi^2 = 0.05$, $P = 0.82$), with the remaining two scans serving as a holdout dataset for the validation analyses presented in Fig. 6. Two scans from different participants were excluded because of incomplete data, resulting in a total of 684 scans for the main analyses. All acquisition parameters and processing pipelines for these data are described in detail elsewhere (*58*–*62*). Bandpass filtering (0.01 to 0.1 Hz) and z scoring were applied to each voxel before time series extraction. The effect of filter settings was investigated in fig. S3. Regional BOLD time series were extracted with the Brainnetome (BNA) atlas (*63*), which includes 246 cortical and subcortical regions of interest (ROIs). Assignment of ROIs to seven canonical RSNs (visual, somatomotor, dorsal attention, ventral attention, default mode, frontoparietal, and limbic) is provided with the BNA template (*63*). This mapping is derived from the cortical network parcellation by Yeo *et al.* (*13*) and is available from www.brainnetome.org/resource. Regions 165, 177, and 178 (located in the left insular gyrus, left cingulate, and right cingulate, respectively) are not labeled in the template and were manually assigned to the frontoparietal network based on their overlap with the Yeo parcellation. Furthermore, regions in the basal ganglia, thalamus, hippocampus, and amygdala were subsumed as subcortical parcels. Last, we investigated the sensitivity of the observed complexity dynamics to methodological choices of functional parcellation and time series extraction (volumetric versus surface-based extraction of cortical time series). To this end, we compared the BNA parcellation to two volumetric atlases of higher and lower spatial granularity [after Shen and colleagues (*64*) with 268 ROIs and after Shirer *et al.* (*65*) with 90 ROIs] as well as to the surface-based multi-modal parcellation (MMP) atlas with 360 cortical ROIs after Glasser and colleagues (*66*), yielding highly convergent results (figs. S4 and S5).

Time-resolved estimation of signal complexity

Signal complexity of BOLD activity was calculated as WPE through symbolic encoding of the time series vectors (*29*). WPE is an amplitude-sensitive extension of permutation entropy (PE) (*67*), an information-theoretic quantity that captures the degree of pattern irregularity as the Shannon entropy (*68*) on the occurrence of symbolic motifs within a time series.

WPE is defined as

$$H_{\mathrm{WPE}}(m,\tau) = -\sum_{i:\pi_i^{m,\tau}\in\pi} p_{\mathrm{w}}(\pi_i^{m,\tau})\ln p_{\mathrm{w}}(\pi_i^{m,\tau}) \quad (1)$$

where m is the length of symbolic motifs in the time series, τ is a lag parameter indicating the number of time points to shift along the time series, $\pi_i^{m,\tau}$ represents the i'th symbolic motif out of the set of possible motifs Π given the motif length, and $p_{\mathrm{w}}(\pi_i^{m,\tau})$ is the variance-weighted relative frequency of motif i, as detailed by Fadlallah and colleagues (*29*). Following methodological considerations (*29*, *69*) and previous applications of WPE to neural data analysis (*70*, *71*), a motif length of m = 3 and a lag parameter of τ = 1 were applied to compute the motif distribution over the signal vector of interest, and WPE values were normalized to lie in [0,1] (*29*). Notably, by leveraging both pattern diversity (assessed by PE) and amplitude information (assessed by the SD over the BOLD vector), WPE captures signal dynamics that remain undetected when considering only one of these characteristics (figs. S1 and S2). A further advantage of WPE lies in its ability to accommodate a time-resolved approach, based on the comparatively low number of time series samples needed to achieve stable estimation (*69*, *72*). Accordingly, we here applied a sliding window approach, where the entire BOLD time series is divided into temporally contiguous windows of a prespecified length and overlap. In the main text, we report the findings for a window length of 60 TRs (43.2 s) with 95% overlap, yielding a window-to-window temporal resolution of 3 TRs (2.16 s) and a time-resolved signal complexity vector of 380 windows. To investigate the sensitivity of the observed complexity dynamics to the windowing parameters, we analyzed window lengths of 60, 90, and 120 samples with 95% and 90% window overlap, respectively, yielding highly convergent results (fig. S4).

Given the ubiquitously observed pattern of predominant high complexity with recurrent complexity drops, we defined a threshold of drop engagement as the first percentile of the total WPE distribution (critical WPE = 0.273; see Fig. 6). Accordingly, whenever a region's signal complexity met this value for a given BOLD window, it was counted as exhibiting a complexity drop in that window (Fig. 1A). Notably, whether this thresholding procedure was applied across all participants or as participant-specific percentile thresholds made essentially no difference to the spatial distribution of where complexity drops occurred (r = 0.99, $P < 0.001$). We then investigated to which extent brain regions coincide in their drop engagement over time. To this end, we iterated over all BOLD windows in the dataset and counted those regions that met the drop threshold simultaneously in each window. This count matrix was normalized by the maximum coincidence count, yielding drop coincidence values from 0 to 1. The pairwise drop coincidences between any two regions were then subjected to correlation analyses with the corresponding FC values (Fig. 1C). Furthermore, we calculated the time-resolved drop affinity for each scan to investigate how the likelihood of exhibiting a complexity drop is distributed over brain regions and age groups. To this end, a binary matrix (BOLD windows over ROIs) was created, containing ones whenever a region's signal complexity met the drop threshold in a particular window, and zero otherwise. These affinity matrices were then averaged to estimate participant-wise and region-wise drop affinity.

Note that the time-resolved affinity vector for individual scans also served the observation of brain-wide engagement in complexity drops (Fig. 2A) and the subsequent propagation analysis.

We furthermore assessed the degree of similarity between a region's complexity time series and its contralateral equivalent (Fig. 1D). To this end, we defined an interhemispheric symmetry index (ISI), which is computed as the correlation coefficient of a region with its contralateral equivalent, weighted by the proportion of the 246 BNA regions that were less strongly correlated with that region. Accordingly, a region with high cross-hemispheric similarity shows many regions that are less correlated with it than the contralateral equivalent, yielding a weighting factor close to one. In contrast, if there are many regions that exhibit a higher correlation to the target region than the contralateral ROI, this weighting factor decreases, resulting in lower ISI values.

Descriptive statistics

Group-level comparisons (e.g., by age or by RSNs) were carried out with the nonparametric Kruskal-Wallis test (*73*), which rests on observation ranks and applies to $n > 2$ groups. Effects were considered statistically significant at a level of $\alpha = 0.05$ for all tests. Pairwise comparisons were conducted with rank sum tests (*74*), adjusting for multiple comparisons using the false discovery rate (FDR). Associations between continuous variables were assessed with parametric or nonparametric correlation tests, depending on the underlying distributions. Participant age as provided in the HCP data was given in the age groups of 22 to 25, 26 to 30, 31 to 35, and >35 years; for age-wise comparisons, however, participants over 35 years were excluded, as this only applied to $n = 3$ individuals. For all assessments of directional effects, two-tailed tests were applied.

Propagation analysis

The propagation of complexity drops across the brain was formalized as a graph theoretical problem. Here, each individual propagation was modeled as a directed graph where nodes represent brain regions exhibiting a complexity drop and directed edges represent the progression in time from one BOLD window to the next.

To identify drop cascades in the dataset, a stepwise search procedure was applied. First, all BOLD windows with at least $n = 10$ regions simultaneously exhibiting a complexity drop were identified in the time-resolved affinity vector. If there were several temporally contiguous windows that met this criterion, the window with the maximum number of dropping regions was defined as the peak layer in the directed graph. From this peak layer, a window-by-window backward and forward search identified the neighboring windows in which the number of dropping regions increased until reaching the peak layer (propagation phase) and decreased after the peak (fade phase), respectively. The minimum cascade length thus included three contiguous windows (initialization-peak-fade). Although very rare, instances in which the windows directly before or after the peak showed no dropping regions were discarded. To investigate the spread of complexity drops in the propagation phase, individual directed graphs were constructed from the initialization window—in which the regions exhibiting drops represent the graph's source nodes—to the peak window (Fig. 2B).

For all windows from initialization to peak, the newly dropping regions from one window to the next were registered to compute the empirical transition probability, where all newly dropping regions in window i obtain directed edges to all newly dropping regions in window $i + 1$. The region-by-region transition probability matrix (TPM) was then constructed on the basis of the path-weighted edges in the propagation graph. Here, edges in temporally contiguous windows were assigned a weight of 1, while connections in non-neighboring windows were assigned the inverse of the path length (e.g., $^1/_2$ for connections from window i to window $i + 2$) to account for the temporal evolution of the spread. For instance, if engagement of region A is frequently followed by engagement of region B, but through variable intermediate engagement of regions C, D, etc., this is missed in a binary TPM, as only neighboring windows are considered. Construction of propagation graphs and TPMs over individual cascades subsequently allowed for participant-wise and group-level analyses: To capture cascade origination, the source node probability of each brain region was computed as the rate of occurrence in the initialization window. The diversity of source nodes was calculated as the percentage of unique brain regions ever initializing a participant's cascades. The average TPM over individual spreads yielded the directed group-level propagation network in Fig. 2E, representing the 95th percentile of path-weighted transition probabilities. However, fig. S14 shows the unthresholded matrix and furthermore illustrates that these spatiotemporal propagation pathways are highly consistent over different peak thresholds (i.e., the minimum number of regions that simultaneously show a complexity drop in the peak window).

Graph construction and topological analyses on the propagation network were implemented with the igraph package (version 1.2.5) for R (*75*). The hub structure of the thresholded network was quantified as Kleinberg centrality, an extension of eigenvector centrality for directed networks (*76*). Geodesic distances were computed for every node-to-node comparison in the temporal propagation network and averaged for all combinations within and across RSNs. The average distance matrix was then subjected to hierarchical clustering using the default complete linkage method (*77*). As this approach revealed a highly suggestive order from unimodal to transmodal networks, we explicitly investigated this cluster structure by defining a unimodal and a transmodal cluster group, subsequently tested with a Monte Carlo simulation using the sigclust package (*78*). The null hypothesis of this cluster test is that the data emanate from a single Gaussian distribution. To assess this hypothesis, 5000 Gaussian samples were created to estimate the distribution of the cluster index (*78*), a test statistic defined as the sum of within-class sums of squares about the mean in relation to the total sum of squares about the overall mean (see https://rdrr.io/cran/sigclust/man).

Clustering of complexity states

The time-resolved signal complexity matrix (rows: 684 scans × 380 windows = 259,920 observations; columns: 246 ROIs) was subjected to unsupervised structure detection to investigate temporally discrete complexity states. To this end, we applied the MATLAB-inbuilt k-means clustering algorithm with a maximum of 1000 iterations, 20 replicates with random initial positions to avoid local minima, the k-means ++ heuristic for centroid initialization, and the squared Euclidean distance as the target metric to be optimized.

On the basis of the observed complexity dynamics (Fig. 1A; online repository: https://osf.io/mr8f7), we expected a predominant

high-complexity state, an infrequent low-complexity state, and a varying number of intermediate complexity states. As common cluster evaluation indices to determine the optimal k of expected clusters resulted in heterogeneous estimates between $k = 3$ and $k = 5$ depending on windowing parameters and the optimization criterion applied, we specified $k = 4$ (i.e., two intermediate complexity states) and ran comprehensive validation analyses for $k = 3$ (i.e., one intermediate state) and $k = 5$ (i.e., three intermediate states). Results reported in the main text were extremely robust against the choice of k, including the occupancy-complexity relationship, the impact of complexity states on network strength and topology, state dispersion, and the spatial topology of complexity states [whose spatial heterogeneity was assessed on the basis of the MLRT (*79*)] and its link to myelination and the primary FC gradient (figs. S8 and S9).

State dispersion index

To assess the degree to which the empirical state visits of an individual participant were distributed across the k possible complexity states, we defined a state dispersion index(SDI), calculated as

$$\mathrm{SDI}(p_k) = 1 - \frac{W_1(p_k, u_k)}{W_1(\delta_k, u_k)} \quad (2)$$

where $W_1(p_k, u_k)$ corresponds to the first Wasserstein distance (*80*, *81*) between the empirically observed discrete distribution of state occupancy p_k (Fig. 3, A to C) and the theoretical maximum dispersion distribution $u_k = U(1, k)$, i.e., the uniform distribution in which each state is visited with a frequency of $1/k$. The Wasserstein metric is also known as the earth mover′s distance and can be viewed as the minimum cost of transforming one probability distribution into another one (or, intuitively, how much a pile of "earth" would need to be moved to be turned into another one). Here, $W_1(p_k, u_k)$ thus describes how much the empirical occupancy distribution would have to be transformed to be maximally dispersed (i.e., identical to the uniform). This distance is normalized by $W_1(\delta_k, u_k)$, which is given by the Wasserstein distance between the theoretical minimum dispersion distribution δ_k (i.e., a zero-entropy degenerate distribution in which only one of the k states is ever visited) and the uniform distribution. Consequently, the SDI lies in [0,1] and is bounded by 0 if only one state was ever visited by the participant (minimum state exploration) and 1 if the empirical state occupancy is identical to the uniform (maximum state exploration).

Distance across complexity states

To characterize the spatial topology across the estimated complexity states, we defined an index of distance across complexity states (DACS). Let K denote the set of unique centroid pairs (i, j) in k-dimensional state space. For each brain region, the DACS is computed as the cumulative Euclidean distance D over all pairs of centroids C in K

$$\mathrm{DACS} = \sum_{(i,j)\in K} D(C_i \| C_j) \quad (3)$$

For the BNA parcellation, this yields a 1×246 vector, where higher values indicate brain regions that show greater centroid-to-centroid distances and thus more pronounced differences in signal complexity over the estimated complexity states. Note that the resulting DACS topology was very robust against the choice of k (figs. S8 and S9) and that this vector constituted the input for the subsequent correlation analyses linking state topology to cortical myelination and the primary FC gradient as well as to structure-function coupling (see below).

FC and network topology

Static FC was estimated as the ROI-by-ROI Pearson correlation matrix over the entire resting-state recording. These matrices were averaged over runs and participants to obtain the group-level FC matrix for investigating the association to drop coincidence and for the construction of the macroscale connectivity gradient. Furthermore, dynamic FC was computed as the correlation matrix over each BOLD window, resulting in a $246 \times 246 \times 380$ array for the specified window parameters. Dynamic connectivity strength was calculated as the mean over these window-wise matrices, yielding a 1×380 vector. The topology of the time-resolved functional networks was assessed with the Brain Connectivity Toolbox (*82*), available from www.brain-connectivity-toolbox.net. Network modularity as a measure of functional segregation was estimated through Louvain community detection (community_louvain.m) with asymmetric treatment of negative weights as previously recommended (*82*) and with a γ parameter of 1.05 to accommodate the ability to detect smaller modules (*82*), reflecting the idea to approximate the number of canonical functional networks with the identified modules. However, modularity estimation was highly consistent across choices of γ values (main text versus toolbox default of $\gamma = 1$: $\rho = 0.99$, $P < 0.001$; all pairwise correlations in linear grid search from $\gamma = 0.75, 0.80, \ldots, 1.25$ yielded ρ coefficients of 0.95 or above). Furthermore, global efficiency as an estimate of functional integration was computed using the efficiency_wei.m function, with negative weights discarded (*82*). This approach yielded vectors of time-resolved modularity and global efficiency (1×380 BOLD windows) for each resting-state recording. These time-resolved vectors constituted the input for the calculation of both the participant averages (Fig. 3A) and the window-to-window transitions (Fig. 3B) of these network measures, where the corresponding complexity state vector from the clustering output served as a state-wise mask.

Computing BOLD cofluctuations

BOLD cofluctuations among brain regions were estimated from the edge time series first introduced by Esfahlani and colleagues (*30*). In brief, this approach entails an exact mathematical decomposition of the correlation between two z-scored time series, which is achieved by omitting the calculation of the mean of their element-wise product and instead yields a time-resolved vector of moment-to-moment cofluctuations of the two regions that can be interpreted as the framewise contribution to their correlation. To compute these cofluctuation time series in our data, we used the code provided by the authors, publicly available from https://github.com/brain-networks/edge-ts. Furthermore, we also followed Esfahlani and colleagues in computing the cofluctuation magnitude as the root sum of squares (RSS) and thresholding RSS time series to the 95th percentile to obtain high-amplitude cofluctuation events. Figure S6 shows an example of these BOLD cofluctuations as computed from our data. Moreover, the cofluctuation of complexity time series shown in fig. S6D was computed in analogy, using the same approach on the regional complexity time series. Notably, although the computational operations on the WPE time series are

identical, BOLD edge time series are computed on single frames, while sample points of complexity time series correspond to windows of 60 frames, resulting in a difference in temporal scales. Comparisons between BOLD cofluctuations and complexity dynamics were thus implemented by (i) comparing the magnitude of complexity cofluctuations and the mean BOLD cofluctuation magnitude per window with continuous correlations (Pearson's r) and (ii) comparing the binary event time series relating whether a drop coincidence was present in a given window and whether a high-amplitude BOLD cofluctuation was present in a given window with biserial correlations (Φ coefficient). While the analyses in fig. S6 rest on pairwise comparisons between the BOLD time series and complexity time series of any two given regions, we also related global BOLD cofluctuation magnitude—computed as the RSS time series across the entire network (*30*)—to global signal complexity and the global number of complexity drops across the whole brain, which similarly yielded limited associations (mean correlation $r = -0.28 \pm 0.14$ for global signal complexity; $r = 0.08 \pm 0.13$ for global complexity drops; $n = 684$ scans).

Null model estimation

Given the ubiquitous observation of complexity drops across participants, scanning sessions, and a range of methodological parameters, we investigated whether the empirical complexity dynamics would be equivalently observed in a null model of temporal dependency displayed in fig. S7. To this end, individual BOLD time series were temporally permuted in blocks of three time points (corresponding to the length of individual motifs), equivalently applied to all regions and scans. This approach preserved the mean and variance of individual time series as well as the covariance structure across time series (i.e., the static FC matrix). The surrogate distribution of signal complexity was then estimated by computing the window-wise WPE values, as detailed above for the empirical data. Since complexity drops are defined as instances equal or below the first percentile of the overall complexity distribution, applying the same threshold to the surrogate distribution ensured that the identical number of "surrogate drops" was present in the null model. This approach subsequently allowed us to ask whether enforcing the presence of these instances would also maintain the spatiotemporal structure and interindividual differences observed in the empirical data. Regarding the spatial topology of signal complexity, we first computed the complexity distribution across brain regions for each scan and related the empirical z scores to the surrogate z scores in fig. S7C. Next, we computed the affinity for complexity drops of individual participants in the surrogate data (fig. S7D) and tested whether the age effect of decreasing drop affinity in higher age was equally found as in the empirical data (Fig. 1B). Last, we asked whether an identical number of drops in the surrogate data would also entail the same propensity of brain regions to drop together (fig. S7E). To this end, we computed the number of drop coincidences per scan and compared them between empirical and surrogate data (rank sum test) and furthermore compared the spatial distribution of which brain regions preferentially drop together, corresponding to the drop coincidence values in Fig. 1C.

Structural connectivity estimation

Structural connectivity matrices were computed using probabilistic tractography as implemented in the FMRIB's Diffusion Toolbox ProbtrackX GPU program (*83*). Diffusion-weighted data provided as the Diffusion BedpostX package were available for 340 of the 343 participants in the study population. These data were preprocessed as previously described (*58*), including registration to native space, movement and eddy current correction, and application of BedpostX to model white matter (WM) fiber orientations for probabilistic tractography. The connectivity distribution is then computed using iterations of streamlines propagated from seed regions to target regions. Briefly, a single propagation entails moving along a streamline by steps of a specified length, evaluating for exclusion or termination criteria at each step, and continuing this process until criteria for exclusion (streamline discarded) or termination (propagation ended but streamline retained) are met. The output is a matrix that quantifies the number of nondiscarded streamlines between a seed and target.

In line with the functional analyses, BNA regions were specified as seed ROIs to guide tractography. Network mode was applied in ProbtrackX to compute an ROI-by-ROI connectivity matrix, where rows represent seed ROIs and columns correspond to target ROIs. Each BNA region was input as a binary mask in MNI space. Since the seed ROIs (standard) and processed diffusion data (native) were not registered to the same space, bidirectional participant-specific nonlinear transformations between standard and structural space as provided by the HCP were passed to ProbtrackX. Following the recommendation that the inclusion of additional anatomical priors increases the biological plausibility of modeled WM tracts (*84*), we included participant-specific gray matter (GM) masks from FreeSurfer as termination masks (--stop). By terminating a propagated streamline as soon as it enters this GM mask, streamlines are forced to terminate near the boundary between GM and WM instead of traveling further into a GM region. Streamline termination parameters were applied as per ProbtrackX defaults: Streamline curvature threshold exceeded (0.2, ~80°), streamline path returns to a point that it already intersected previously (--loopcheck), streamline exits nodiff_brain_mask (BedpostX output), and maximum number of steps per streamline (2000) reached using a step length of 0.5 mm.

For each voxel in a seed region, 1000 samples were propagated. Distance correction (--pd) was applied to compensate for the bias that the probability of a streamline successfully reaching the target ROI decreases as the distance between a seed and target ROI increases. Distance correction as implemented in ProbtrackX adjusts the connectivity distribution between a seed-target ROI pair by multiplying the number of successful streamlines between the ROIs by the average path length of the streamlines. Last, ROI-by-ROI connectivity matrices were then normalized using the probabilistic streamline connectivity index (PSCI) procedure, as previously described (*85*). The PSCI scales the streamline counts between ROI pairs based on the number of propagated and successful streamlines as well as the size of both the seed and target ROIs.

Estimating structure-function coupling

Structure-function coupling was estimated with the structural-decoupling index introduced by Preti and Van De Ville (*41*). Here, we refer to this measure as the Structure-Function Decoupling Index (SFDI) to avoid confusion of the acronym with the SDI detailed above. The SFDI quantifies the dependency of functional signals on anatomical structure and builds upon a series of concepts from graph harmonic analysis. In brief, the structural connectome is

decomposed into harmonic components, and brain activity of every time point is written as a weighted linear combination of harmonic components. A key step entails a splitting procedure that decomposes brain activity into coupled and uncoupled portions, and the ratio of decoupled and coupled signal norms then yields the SFDI. To estimate SFDI values from our data, we used the code provided by the authors at www.github.com/gpreti/GSP_StructuralDecouplingIndex. The regional SFDI values displayed in Fig. 5A correspond to the average across scans and are displayed in binary logarithmic scale, as in (*41*). We then related the degree of structure-function coupling per region to the DACS by means of a spin permutation test, as detailed below.

Myelin estimation

Cortical grayordinate myelin maps obtained from the T1-weighted/T2-weighted image ratios (*53*) were used to calculate the average myelin content of ROIs in the atlas template. Since our parcellation approach did not benefit from the higher resolution of the 164k images, we analyzed the unsmoothed, bias-corrected 32k areal feature–based aligned images ("MyelinMap_BC_MSMAll.32k_fs_LR.dscalar.nii") using the Multimodal Surface Matching algorithm (*86*). Parcel-wise myelin content was obtained using the Connectome Workbench (command: -cifti-parcellate) by averaging over the myelin map within the respective BNA regions.

Gradient construction, spin permutation, and hierarchical regression

The macroscale connectivity gradient was computed on the group-average FC matrix. As only the cortex is mapped to the FreeSurfer sphere for later spin permutation, the input matrix was restricted to the 210 × 210 cortical ROIs of the BNA. Gradient analysis was implemented with the BrainSpace toolbox (*87*) for neuroimaging and connectomic datasets. Following Margulies and colleagues (*23*), cosine similarity was applied to compute the affinity matrix. A total of 10 components, diffusion embedding for nonlinear dimensionality reduction (diffusion time of 0, α parameter of 0.5), and 90% region-wise feature sparsity were used for gradient construction, following the default recommendations (*87*). The gradient fit on these data is displayed in Fig. 4C and precisely identified the principal unimodal-to-transmodal connectivity gradient first reported by Margulies and colleagues (*23*). To examine the association between these gradient loadings and the other cortical features (myelination and DACS), we applied spin permutation correlation of the respective cortical maps. This approach consists in a series of random spherical rotations that preserve the spatial autocorrelation of the data, resulting in empirical null models that counteract the potential inflation of statistical significance in simple univariate tests (*87*–*89*). Here, we implemented a variant of this procedure that specifically applies to parcellated instead of vertex-wise cortical maps (*90*). Nonparametric correlations over 5000 random rotations were computed to estimate the empirical distribution of the test statistic for the three comparisons between gradient loadings, cortical myelination, and the DACS described above.

The empirically observed associations across these cortical features were furthermore subjected to a nonparametric partial correlation analysis using the ppcor package for R (Fig. 4D) (*91*). As this approach suggested high explanatory power of complexity states, these analyses were corroborated with a hierarchical regression approach, where variance in gradient loadings was modeled as a function of cortical myelination (compact model 1), the DACS (compact model 2), or both (augmented model 3). These individual linear models were then compared through *F* tests for nested models with the lmSupport package for R (https://rdrr.io/cran/lmSupport).

Complexity-behavior associations

To assess associations between signal complexity and participant characteristics, average WPE values per ROI and participant were tested against age and indices of cognitive performance, motor skills, and sensory scores, as provided with the HCP data. To ensure data quality and to minimize the impact of non-normally distributed variables, we transformed response time data to speed via inversion, subjected skewed data to log transformations (if absolute skewness >1), excluded data from participants with missing values in at least one variable, and removed outliers (mean ± 4 SDs). In total, data from 13 participants were thus excluded, leaving n = 330 participants for behavioral analyses. To this end, we tested the multivariate relationship between BOLD signal complexity and individual participant measures by means of a PLS analysis (Fig. 7) (*92*–*94*). We applied a behavioral PLS approach that allows for the estimation of multivariate correlations between a three-dimensional brain variable (average WPE per ROI and participant) and multiple behavioral measures (fig. S12). To focus this analysis on general features of behavioral and cognitive abilities, we performed principal component analyses on the respective sets of single measures of performance and speed in cognitive tasks, motor performance, and sensory skills. For each of the four domains, the first principal component accounted for more than 35% of the total variance, and component loadings were strictly positive, resulting in four principal component scores per participant that entered PLS analyses alongside individual age as well as composite scores of fluid and crystalized cognition, as provided with the HCP data, such that seven behavioral variables were used in the PLS analysis.

In brief, PLS works via the calculation of a correlation matrix that captures the between-participant correlation of the target brain measure in each region and the behavioral metrics of interest (matrix size: $N_{regions} \times N_{behavior} = 246 \times 7$). Next, this rank correlation matrix is decomposed using singular value decomposition, resulting in $N_{behavior} \times N_{behavior}$ latent variables. This approach produces two main outputs: (i) a singular value for every latent variable, indicating the proportion of cross-block variance explained by the latent variable, and (ii) a pattern of weights ($N_{regions}$) representing the rank correlation strength between WPE and behavioral measures. The multiplication (dot product) of these weights with region-wise WPE yields brain scores reflecting the between-participant correlation of complexity and behavioral metrics. Statistical significance of these brain scores and underlying latent variables was tested by permuting behavioral measures across participants and recalculating the singular value of each latent variable (5000 permutations). To furthermore estimate the robustness of the calculated weights, a bootstrap procedure was applied (5000 bootstraps with replacement). The division of the empirical weights by the bootstrapped standard error yields bootstrap ratios (BSRs). These BSR values estimate the robustness of observed effects on a region-wise level and can be interpreted as values from a *z*-distribution. Hence, BSR values exceeding 1.96 relate to a correlation between the latent brain scores (weighted average WPE) and the

latent behavioral scores (weighted behavioral metrics) at $P < 0.05$, and likewise $P < 0.01$ for BSR values exceeding 2.7. Moreover, bootstrap resampling was also applied to estimate the 95% confidence intervals for the observed indicator correlations between WPE and behavioral measures. As noted in the main text, this approach was conducted separately for the main and holdout datasets as well as for individual scanning sessions to estimate the robustness of complexity-behavior effects, with highly consistent results (Fig. 7 and fig. S13).

Supplementary Materials

This PDF file includes:
Figs. S1 to S14

Other Supplementary Material for this manuscript includes the following:
Movie S1

View/request a protocol for this paper from *Bio-protocol*.

REFERENCES AND NOTES

1. D. S. Bassett, O. Sporns, Network neuroscience. *Nat. Neurosci.* **20**, 353–364 (2017).
2. J. D. Power, A. L. Cohen, S. M. Nelson, G. S. Wig, K. A. Barnes, J. A. Church, A. C. Vogel, T. O. Laumann, F. M. Miezin, B. L. Schlaggar, S. E. Petersen, Functional network organization of the human brain. *Neuron* **72**, 665–678 (2011).
3. E. Bullmore, O. Sporns, Complex brain networks: Graph theoretical analysis of structural and functional systems. *Nat. Rev. Neurosci.* **10**, 186–198 (2009).
4. N. U. F. Dosenbach, D. A. Fair, F. M. Miezin, A. L. Cohen, K. K. Wenger, R. A. T. Dosenbach, M. D. Fox, A. Z. Snyder, J. L. Vincent, M. E. Raichle, B. L. Schlaggar, S. E. Petersen, Distinct brain networks for adaptive and stable task control in humans. *Proc. Natl. Acad. Sci. U.S.A.* **104**, 11073–11078 (2007).
5. M. D. Fox, A. Z. Snyder, J. L. Vincent, M. Corbetta, D. C. Van Essen, M. E. Raichle, The human brain is intrinsically organized into dynamic, anticorrelated functional networks. *Proc. Natl. Acad. Sci. U.S.A.* **102**, 9673–9678 (2005).
6. M. D. Fox, M. E. Raichle, Spontaneous fluctuations in brain activity observed with functional magnetic resonance imaging. *Nat. Rev. Neurosci.* **8**, 700–711 (2007).
7. M. E. Raichle, A. M. MacLeod, A. Z. Snyder, W. J. Powers, D. A. Gusnard, G. L. Shulman, A default mode of brain function. *Proc. Natl. Acad. Sci. U.S.A.* **98**, 676–682 (2001).
8. D. C. Van Essen, S. M. Smith, D. M. Barch, T. E. J. Behrens, E. Yacoub, K. Ugurbil; WU-Minn HCP Consortium, The WU-Minn human connectome project: An overview. *Neuroimage* **80**, 62–79 (2013).
9. A. Fornito, A. Zalesky, M. Breakspear, The connectomics of brain disorders. *Nat. Rev. Neurosci.* **16**, 159–172 (2015).
10. B. Biswal, F. Zerrin Yetkin, V. M. Haughton, J. S. Hyde, Functional connectivity in the motor cortex of resting human brain using echo-planar MRI. *Magn. Reson. Med.* **34**, 537–541 (1995).
11. A. T. Reid, D. B. Headley, R. D. Mill, R. Sanchez-Romero, L. Q. Uddin, D. Marinazzo, D. J. Lurie, P. A. Valdés-Sosa, S. J. Hanson, B. B. Biswal, V. Calhoun, R. A. Poldrack, M. W. Cole, Advancing functional connectivity research from association to causation. *Nat. Neurosci.* **22**, 1751–1760 (2019).
12. A. Zalesky, A. Fornito, E. Bullmore, On the use of correlation as a measure of network connectivity. *Neuroimage* **60**, 2096–2106 (2012).
13. B. T. Yeo, F. M. Krienen, J. Sepulcre, M. R. Sabuncu, D. Lashkari, M. Hollinshead, J. L. Roffman, J. W. Smoller, L. Zöllei, J. R. Polimeni, The organization of the human cerebral cortex estimated by intrinsic functional connectivity. *J. Neurophysiol.* **106**, 1125–1165 (2011).
14. E. A. Allen, E. Damaraju, S. M. Plis, E. B. Erhardt, T. Eichele, V. D. Calhoun, Tracking whole-brain connectivity dynamics in the resting state. *Cereb. Cortex* **24**, 663–676 (2014).
15. V. D. Calhoun, R. Miller, G. Pearlson, T. Adalı, The chronnectome: Time-varying connectivity networks as the next frontier in fMRI data discovery. *Neuron* **84**, 262–274 (2014).
16. C. Chang, G. H. Glover, Time-frequency dynamics of resting-state brain connectivity measured with fMRI. *Neuroimage* **50**, 81–98 (2010).
17. X. Liu, J. H. Duyn, Time-varying functional network information extracted from brief instances of spontaneous brain activity. *Proc. Natl. Acad. Sci. U.S.A.* **110**, 4392–4397 (2013).
18. A. Zalesky, A. Fornito, L. Cocchi, L. L. Gollo, M. Breakspear, Time-resolved resting-state brain networks. *Proc. Natl. Acad. Sci. U.S.A.* **111**, 10341–10346 (2014).
19. S. Achard, E. Bullmore, Efficiency and cost of economical brain functional networks. *PLOS Comput. Biol.* **3**, e17 (2007).
20. E. Bullmore, O. Sporns, The economy of brain network organization. *Nat. Rev. Neurosci.* **13**, 336–349 (2012).
21. J. M. Shine, O. Koyejo, R. A. Poldrack, Temporal metastates are associated with differential patterns of time-resolved connectivity, network topology, and attention. *Proc. Natl. Acad. Sci. U.S.A.* **113**, 9888–9891 (2016).
22. J. M. Huntenburg, P.-L. Bazin, D. S. Margulies, Large-scale gradients in human cortical organization. *Trends Cogn. Sci.* **22**, 21–31 (2018).
23. D. S. Margulies, S. S. Ghosh, A. Goulas, M. Falkiewicz, J. M. Huntenburg, G. Langs, G. Bezgin, S. B. Eickhoff, F. X. Castellanos, M. Petrides, E. Jefferies, J. Smallwood, Situating the default-mode network along a principal gradient of macroscale cortical organization. *Proc. Natl. Acad. Sci. U.S.A.* **113**, 12574–12579 (2016).
24. G. Shafiei, R. D. Markello, R. Vos de Wael, B. C. Bernhardt, B. D. Fulcher, B. Misic, Topographic gradients of intrinsic dynamics across neocortex. *eLife* **9**, e62116 (2020).
25. G. Baracchini, B. Mišić, R. Setton, L. Mwilambwe-Tshilobo, M. Girn, J. S. Nomi, L. Q. Uddin, G. R. Turner, R. N. Spreng, Inter-regional BOLD signal variability is an organizational feature of functional brain networks. *Neuroimage* **237**, 118149 (2021).
26. G. Deco, V. K. Jirsa, A. R. McIntosh, Emerging concepts for the dynamical organization of resting-state activity in the brain. *Nat. Rev. Neurosci.* **12**, 43–56 (2011).
27. J. D. Power, B. L. Schlaggar, S. E. Petersen, Studying brain organization via spontaneous fMRI signal. *Neuron* **84**, 681–696 (2014).
28. L. Q. Uddin, Bring the noise: Reconceptualizing spontaneous neural activity. *Trends Cogn. Sci.* **24**, 734–746 (2020).
29. B. Fadlallah, B. Chen, A. Keil, J. Príncipe, Weighted-permutation entropy: A complexity measure for time series incorporating amplitude information. *Phys. Rev. E Stat. Nonlin. Soft. Matter Phys.* **87**, –022911 (2013).
30. F. Z. Esfahlani, Y. Jo, J. Faskowitz, L. Byrge, D. P. Kennedy, O. Sporns, R. F. Betzel, High-amplitude cofluctuations in cortical activity drive functional connectivity. *Proc. Natl. Acad. Sci. U.S.A.* **117**, 28393–28401 (2020).
31. L. Q. Uddin, An 'edgy' new look. *Nat. Neurosci.* **23**, 1471–1472 (2020).
32. R. Liégeois, B. T. T. Yeo, D. Van De Ville, Interpreting null models of resting-state functional MRI dynamics: Not throwing the model out with the hypothesis. *Neuroimage* **243**, 118518 (2021).
33. A. Mitra, A. Z. Snyder, E. Tagliazucchi, H. Laufs, M. E. Raichle, Propagated infra-slow intrinsic brain activity reorganizes across wake and slow wave sleep. *eLife* **4**, e10781 (2015).
34. R. V. Raut, A. Mitra, S. Marek, M. Ortega, A. Z. Snyder, A. Tanenbaum, T. O. Laumann, N. U. F. Dosenbach, M. E. Raichle, Organization of propagated intrinsic brain activity in individual humans. *Cereb. Cortex* **30**, 1716–1734 (2020).
35. B. Vézquez-Rodríguez, Z.-Q. Liu, P. Hagmann, B. Misic, Signal propagation via cortical hierarchies. *Netw. Neurosci.* **4**, 1072–1090 (2020).
36. J. M. Huntenburg, P.-L. Bazin, A. Goulas, C. L. Tardif, A. Villringer, D. S. Margulies, A systematic relationship between functional connectivity and intracortical myelin in the human cerebral cortex. *Cereb. Cortex* **27**, 981–997 (2017).
37. J. B. Burt, M. Demirtaş, W. J. Eckner, N. M. Navejar, J. L. Ji, W. J. Martin, A. Bernacchia, A. Anticevic, J. D. Murray, Hierarchy of transcriptomic specialization across human cortex captured by structural neuroimaging topography. *Nat. Neurosci.* **21**, 1251–1259 (2018).
38. L. E. Suárez, R. D. Markello, R. F. Betzel, B. Misic, Linking structure and function in macroscale brain networks. *Trends Cogn. Sci.* **24**, 302–315 (2020).
39. B. D. Fulcher, J. D. Murray, V. Zerbi, X.-J. Wang, Multimodal gradients across mouse cortex. *Proc. Natl. Acad. Sci. U.S.A.* **116**, 4689–4695 (2019).
40. J. M. Huntenburg, L. Y. Yeow, F. Mandino, J. Grandjean, Gradients of functional connectivity in the mouse cortex reflect neocortical evolution. *Neuroimage* **225**, 117528 (2021).
41. M. G. Preti, D. Van De Ville, Decoupling of brain function from structure reveals regional behavioral specialization in humans. *Nat. Commun.* **10**, 4747 (2019).
42. L. Waschke, N. A. Kloosterman, J. Obleser, D. D. Garrett, Behavior needs neural variability. *Neuron* **109**, 751–766 (2021).
43. M. Pope, M. Fukushima, R. F. Betzel, O. Sporns, Modular origins of high-amplitude cofluctuations in fine-scale functional connectivity dynamics. *Proc. Natl. Acad. Sci. U.S.A.* **118**, e2109380118 (2021).
44. Z. Ladwig, B. A. Seitzman, A. Dworetsky, Y. Yu, B. Adeyemo, D. M. Smith, S. E. Petersen, C. Gratton, BOLD cofluctuation 'events' are predicted from static functional connectivity. *Neuroimage* **260**, 119476 (2022).
45. J. Faskowitz, F. Z. Esfahlani, Y. Jo, O. Sporns, R. F. Betzel, Edge-centric functional network representations of human cerebral cortex reveal overlapping system-level architecture. *Nat. Neurosci.* **23**, 1644–1654 (2020).

46. D. S. Bassett, N. F. Wymbs, M. A. Porter, P. J. Mucha, J. M. Carlson, S. T. Grafton, Dynamic reconfiguration of human brain networks during learning. *Proc. Natl. Acad. Sci. U.S.A.* **108**, 7641–7646 (2011).
47. O. Sporns, The complex brain: Connectivity, dynamics, information. *Trends Cogn. Sci.* **26**, 1066–1067 (2022).
48. A. Mitra, M. E. Raichle, How networks communicate: Propagation patterns in spontaneous brain activity. *Philos. Trans. R Soc. Lond. B Biol. Sci.* **371**, 20150546 (2016).
49. G. Deco, M. L. Kringelbach, Hierarchy of information processing in the brain: A novel 'intrinsic ignition' framework. *Neuron* **94**, 961–968 (2017).
50. G. Deco, D. Vidaurre, M. L. Kringelbach, Revisiting the global workspace orchestrating the hierarchical organization of the human brain. *Nat. Hum. Behav.* **5**, 497–511 (2021).
51. R. V. Raut, A. Z. Snyder, A. Mitra, D. Yellin, N. Fujii, R. Malach, M. E. Raichle, Global waves synchronize the brain's functional systems with fluctuating arousal. *Sci. Adv.* **7**, eabf2709 (2021).
52. D. J. Newbold, T. O. Laumann, C. R. Hoyt, J. M. Hampton, D. F. Montez, R. V. Raut, M. Ortega, A. Mitra, A. N. Nielsen, D. B. Miller, B. Adeyemo, A. L. Nguyen, K. M. Scheidter, A. B. Tanenbaum, A. N. Van, S. Marek, B. L. Schlaggar, A. R. Carter, D. J. Greene, E. M. Gordon, M. E. Raichle, S. E. Petersen, A. Z. Snyder, N. U. F. Dosenbach, Plasticity and spontaneous activity pulses in disused human brain circuits. *Neuron* **107**, 580–589.e6 (2020).
53. M. F. Glasser, D. C. Van Essen, Mapping human cortical areas *in vivo* based on myelin content as revealed by T1- and T2-weighted MRI. *J. Neurosci.* **31**, 11597–11616 (2011).
54. F. Váša, B. Mišić, Null models in network neuroscience. *Nat. Rev. Neurosci.* **23**, 493–504 (2022).
55. E. S. Finn, X. Shen, D. Scheinost, M. D. Rosenberg, J. Huang, M. M. Chun, X. Papademetris, R. T. Constable, Functional connectome fingerprinting: Identifying individuals using patterns of brain connectivity. *Nat. Neurosci.* **18**, 1664–1671 (2015).
56. M. Mantwill, M. Gell, S. Krohn, C. Finke, Brain connectivity fingerprinting and behavioural prediction rest on distinct functional systems of the human connectome. *Commun. Biol.* **5**, 261 (2022).
57. E. M. Gordon, T. O. Laumann, A. W. Gilmore, D. J. Newbold, D. J. Greene, J. J. Berg, M. Ortega, C. Hoyt-Drazen, C. Gratton, H. Sun, J. M. Hampton, R. S. Coalson, A. L. Nguyen, K. B. McDermott, J. S. Shimony, A. Z. Snyder, B. L. Schlaggar, S. E. Petersen, S. M. Nelson, N. U. F. Dosenbach, Precision functional mapping of individual human brains. *Neuron* **95**, 791–807.e7 (2017).
58. M. F. Glasser, S. N. Sotiropoulos, J. A. Wilson, T. S. Coalson, B. Fischl, J. L. Andersson, J. Xu, S. Jbabdi, M. Webster, J. R. Polimeni, D. C. Van Essen, M. Jenkinson; WU-Minn HCP Consortium, The minimal preprocessing pipelines for the Human Connectome Project. *Neuroimage* **80**, 105–124 (2013).
59. G. Salimi-Khorshidi, G. Douaud, C. F. Beckmann, M. F. Glasser, L. Griffanti, S. M. Smith, Automatic denoising of functional MRI data: Combining independent component analysis and hierarchical fusion of classifiers. *Neuroimage* **90**, 449–468 (2014).
60. M. Jenkinson, C. F. Beckmann, T. E. J. Behrens, M. W. Woolrich, S. M. Smith, FSL. *NeuroImage.* **62**, 782–790 (2012).
61. B. Fischl, FreeSurfer. *NeuroImage* **62**, 774–781 (2012).
62. M. Jenkinson, P. Bannister, M. Brady, S. Smith, Improved optimization for the robust and accurate linear registration and motion correction of brain images. *Neuroimage* **17**, 825–841 (2002).
63. L. Fan, H. Li, J. Zhuo, Y. Zhang, J. Wang, L. Chen, Z. Yang, C. Chu, S. Xie, A. R. Laird, P. T. Fox, S. B. Eickhoff, C. Yu, T. Jiang, The human brainnetome atlas: A new brain atlas based on connectional architecture. *Cereb. Cortex* **26**, 3508–3526 (2016).
64. X. Shen, F. Tokoglu, X. Papademetris, R. T. Constable, Groupwise whole-brain parcellation from resting-state fMRI data for network node identification. *Neuroimage* **82**, 403–415 (2013).
65. W. R. Shirer, S. Ryali, E. Rykhlevskaia, V. Menon, M. D. Greicius, Decoding subject-driven cognitive states with whole-brain connectivity patterns. *Cereb. Cortex* **22**, 158–165 (2012).
66. M. F. Glasser, T. S. Coalson, E. C. Robinson, C. D. Hacker, J. Harwell, E. Yacoub, K. Ugurbil, J. Andersson, C. F. Beckmann, M. Jenkinson, S. M. Smith, D. C. Van Essen, A multi-modal parcellation of human cerebral cortex. *Nature* **536**, 171–178 (2016).
67. C. Bandt, B. Pompe, Permutation entropy: A natural complexity measure for time series. *Phys. Rev. Lett.* **88**, 174102 (2002).
68. C. E. Shannon, A mathematical theory of communication. *Bell Syst. Tech. J.* **27**, 379–423 (1948).
69. M. Riedl, A. Müller, N. Wessel, Practical considerations of permutation entropy. *Eur. Phys. J. Spec. Top.* **222**, 249–262 (2013).
70. L. Waschke, M. Wöstmann, J. Obleser, States and traits of neural irregularity in the age-varying human brain. *Sci. Rep.* **7**, 17381 (2017).
71. L. Waschke, S. Tune, J. Obleser, Local cortical desynchronization and pupil-linked arousal differentially shape brain states for optimal sensory performance. *eLife* **8**, e51501 (2019).
72. J. Amigó, S. Zambrano, M. A. Sanjuán, Combinatorial detection of determinism in noisy time series. *Europhys. Lett.* **83**, 60005 (2008).
73. W. H. Kruskal, W. A. Wallis, Use of ranks in one-criterion variance analysis. *J. Am. Stat. Assoc.* **47**, 583–621 (1952).
74. F. Wilcoxon, Individual comparisons by ranking methods. *Biometrics* **1**, 80–83 (1945).
75. G. Csardi, T. Nepusz, The igraph software package for complex network research. *Int. J. Complex Syst.* **1695**, 1–9 (2006).
76. J. M. Kleinberg, Authoritative sources in a hyperlinked environment. *J. ACM* **46**, 604–632 (1999).
77. R Core Team, *R: A Language and Environment for Statistical Computing* (R Foundation for Statistical Computing, 2020);www.R-project.org/.
78. Y. Liu, D. N. Hayes, A. Nobel, J. S. Marron, Statistical significance of clustering for high-dimension, low–sample size data. *J. Am. Stat. Assoc.* **103**, 1281–1293 (2008).
79. K. Krishnamoorthy, M. Lee, Improved tests for the equality of normal coefficients of variation. *Comput. Stat.* **29**, 215–232 (2014).
80. S. Kolouri, S. Park, M. Thorpe, D. Slepčev, G. K. Rohde, Optimal mass transport: Signal processing and machine-learning applications. *IEEE Signal Process. Mag.* **34**, 43–59 (2017).
81. L. N. Vaserstein, Markov processes over denumerable products of spaces, describing large systems of automata. *Probl. Peredachi Inf.* **5**, 64–72 (1969).
82. M. Rubinov, O. Sporns, Complex network measures of brain connectivity: Uses and interpretations. *Neuroimage* **52**, 1059–1069 (2010).
83. M. Hernandez-Fernandez, I. Reguly, S. Jbabdi, M. Giles, S. Smith, S. N. Sotiropoulos, Using GPUs to accelerate computational diffusion MRI: From microstructure estimation to tractography and connectomes. *Neuroimage* **188**, 598–615 (2019).
84. C. Yeh, D. K. Jones, X. Liang, M. Descoteaux, A. Connelly, Mapping structural connectivity using diffusion MRI: Challenges and opportunities. *J. Magn. Reson. Imaging* **53**, 1666–1682 (2021).
85. J. A. McNab, B. L. Edlow, T. Witzel, S. Y. Huang, H. Bhat, K. Heberlein, T. Feiweier, K. Liu, B. Keil, J. Cohen-Adad, M. D. Tisdall, R. D. Folkerth, H. C. Kinney, L. L. Wald, The human connectome project and beyond: Initial applications of 300 mT/m gradients. *Neuroimage* **80**, 234–245 (2013).
86. E. C. Robinson, S. Jbabdi, M. F. Glasser, J. Andersson, G. C. Burgess, M. P. Harms, S. M. Smith, D. C. Van Essen, M. Jenkinson, MSM: A new flexible framework for multimodal surface matching. *Neuroimage* **100**, 414–426 (2014).
87. R. Vos de Wael, O. Benkarim, C. Paquola, S. Lariviere, J. Royer, S. Tavakol, T. Xu, S.-J. Hong, G. Langs, S. Valk, B. Misic, M. Milham, D. Margulies, J. Smallwood, B. C. Bernhardt, BrainSpace: A toolbox for the analysis of macroscale gradients in neuroimaging and connectomics datasets. *Commun. Biol.* **3**, 103 (2020).
88. A. F. Alexander-Bloch, H. Shou, S. Liu, T. D. Satterthwaite, D. C. Glahn, R. T. Shinohara, S. N. Vandekar, A. Raznahan, On testing for spatial correspondence between maps of human brain structure and function. *Neuroimage* **178**, 540–551 (2018).
89. A. Alexander-Bloch, A. Raznahan, E. Bullmore, J. Giedd, The convergence of maturational change and structural covariance in human cortical networks. *J. Neurosci.* **33**, 2889–2899 (2013).
90. F. Váša, J. Seidlitz, R. Romero-Garcia, K. J. Whitaker, G. Rosenthal, P. E. Vértes, M. Shinn, A. Alexander-Bloch, P. Fonagy, R. J. Dolan, P. B. Jones, I. M. Goodyer; NSPN Consortium, O. Sporns, E. T. Bullmore, Adolescent tuning of association cortex in human structural brain networks. *Cereb. Cortex* **28**, 281–294 (2018).
91. S. Kim, ppcor: An R package for a fast calculation to semi-partial correlation coefficients. *Commun. Stat. Appl. Methods* **22**, 665–674 (2015).
92. A. McIntosh, F. Bookstein, J. V. Haxby, C. L. Grady, Spatial pattern analysis of functional brain images using partial least squares. *Neuroimage* **3**, 143–157 (1996).
93. A. R. McIntosh, N. J. Lobaugh, Partial least squares analysis of neuroimaging data: Applications and advances. *Neuroimage* **23**, S250–S263 (2004).
94. A. Krishnan, L. J. Williams, A. R. McIntosh, H. Abdi, Partial least squares (PLS) methods for neuroimaging: A tutorial and review. *Neuroimage* **56**, 455–475 (2011).

Acknowledgments: We thank M. Mantwill for assistance in data management and discussions on the present results. **Funding:** This work was supported by German Ministry of Education and Research (BMBF) grant 13GW0206D (S.K. and C.F.); Cusanuswerk foundation (N.v.S.); Berlin School of Mind and Brain (A.R.); German Research Foundation grants IRTG2150 (M.G.), 327654276 (SFB 1315) (C.F.), FI 2309/1-1 (Heisenberg Programme) (C.F.), and FI 2309/2-1 (C.F.); Max Planck UCL Centre for Computational Psychiatry and Ageing Research (L.W. and D.D.G.); and German Research Foundation Emmy Noether Programme (D.D.G.). **Author contributions:** Conceptualization: S.K., N.v.S., and C.F. Data curation: S.K., N.v.S., and A.R. Formal analysis: S.K., N.v.S., L.W., A.R., and M.G. Funding acquisition: D.D.G. and C.F. Investigation: S.K., N.v.S., and L.W. Methodology: S.K., N.v.S., L.W., and D.D.G. Software: S.K., N.v.S., L.W., A.R., and M.G. Supervision: D.D.G. and C.F. Validation: S.K., N.v.S., L.W., and A.R. Visualization: S.K. and N.v.S. Writing—original draft: S.K., N.v.S., L.W., A.R., and M.G. Writing—review and editing: S.K., N.v.S., L.W., A.R.,

M.G., D.D.G., and C.F. **Competing interests:** The authors declare that they have no competing interests. **Data and materials availability:** All data analyzed here are publicly available from the HCP Young Adult dataset of the Human Connectome Project (https://humanconnectome.org/study/hcp-young-adult). Analysis code is available from the corresponding authors and the online repository https://osf.io/mr8f7, which also includes further supporting information such as complexity time series for individual scans and movie S1. All data needed to evaluate the conclusions in the paper are present in the paper and/or the Supplementary Materials.

Submitted 25 April 2022
Accepted 4 January 2023
Published 1 February 2023
10.1126/sciadv.abq3851

ScienceAdvances

A spatiotemporal complexity architecture of human brain activity

Stephan Krohn, Nina von Schwanenflug, Leonhard Waschke, Amy Romanello, Martin Gell, Douglas D. Garrett, and Carsten Finke

Sci. Adv., **9** (5), eabq3851.
DOI: 10.1126/sciadv.abq3851